

## ABSTRACT

MCLAUGHLIN, LETISHA ANNETTE. X-ray Observations of G296.8-0.3. (Under the direction of Dr. Stephen P. Reynolds and Dr. Kazimierz Borkowski.)

Supernova remnants (SNRs) play a central role in the distribution of heavy elements and kinetic energy in their host galaxies. However, studies of these processes are mostly limited to a few well-studied or young SNRs analyzed assuming spherical symmetry. G296.8-0.3, found in the southern constellation Crux, is a very large and asymmetric remnant which may offer insight into the not-so-ideal case of a stellar progenitor exploding into an inhomogeneous medium. Additionally, this remnant has been observed to have faint X-ray emission coincident with the brightest features in radio and infrared energies. I present the ongoing analysis of the peculiar structure of supernova remnant G296.8-0.3, as studied with data collected by the three EPIC telescopes aboard the XMM-Newton X-ray Observatory. The source spectra have been fitted with various models describing the interaction of a strong shock wave with ambient material. Parameters derived from the best fits, not limited to the ionization state, plasma temperature, and elemental abundances, will be used to derive pressures, densities, and other properties of G296.8-0.3.

X-ray Observations of G296.8-0.3

by  
Letisha McLaughlin

A thesis submitted to the Graduate Faculty of  
North Carolina State University  
in partial fulfillment of the  
requirements for the Degree of  
Master of Science

Physics

Raleigh, North Carolina

2010

APPROVED BY:

---

Dr. Stephen P. Reynolds  
Chair of Advisory Committee

---

Dr. Kazimierz Borkowski  
Co-chair of Advisory Committee

---

Dr. Dean Lee

## **DEDICATION**

To my mother for believing I could be greater than  
I ever imagined.

## **BIOGRAPHY**

As a girl who used to look up at the stars from a generic brand, 4-inch refraction telescope, I feel I am one of the privileged few to see her dream lived to its fullest extent. I have enjoyed every step of the way towards this degree, and look forward to the ways in which I will use my knowledge in the future.

## **ACKNOWLEDGEMENTS**

I would like to thank my advisors, Dr. Stephen Reynolds and Dr. Kazimierz Borkowski, for their seemingly limitless knowledge and patience.

## TABLE OF CONTENTS

LIST OF TABLES .....	vii
LIST OF FIGURES .....	viii
LIST OF SYMBOLS .....	x
LIST OF ABBREVIATIONS .....	xi
INTRODUCTION .....	1
A SUMMARY ON SUPERNOVA REMNANTS .....	3
STELLAR ORIGINS .....	5
SNe TYPOLGY .....	13
SNR EVOLUTION .....	16
SNR MORPHOLOGY .....	21
SNRS IN MULTIPLE WAVELENGTHS .....	26
X-RAY EMISSION IN SNRS .....	29
XMM-NEWTON AND SAS .....	32
DATA PROCESSING .....	34
MODELING .....	40
EPIC BACKGROUND .....	42
SNR G296.8-0.3 .....	49
ANALYSIS OF G296.8-0.3 .....	57
FINAL ANALYSIS .....	68
RESULTS .....	76

CONCLUSIONS .....	81
REFERENCES .....	84

**LIST OF TABLES**

Table 1. A summary of G296.8-0.3..... 51

## LIST OF FIGURES

Figure 1. Hertzsprung-Russell diagram .....	6
Figure 2. Burning stages of a core collapse progenitor .....	9
Figure 3. Periodic table of elements .....	11
Figure 4. The anatomy of a supernova remnant.....	18
Figure 5. Limb brightening .....	22
Figure 6. Tycho’s supernova remnant .....	23
Figure 7. The Crab Nebula in radio energies .....	24
Figure 8. The Crab Nebula in infrared, X-ray, and optical energies .....	27
Figure 9. Power law fit with PN spectral response file .....	38
Figure 10. Spatial variation in the quiescent particle backgrounds in MOS .....	44
Figure 11. Quiescent particle background from MOS1 .....	46
Figure 12. Background contributions in PN and MOS .....	48
Figure 13. G296.8-0.3 pictured in other works .....	52
Figure 14. Light curves of two G296.8-0.3 observations .....	58
Figure 15. G296.8-0.3 in <i>XMM-Newton</i> observations .....	59
Figure 16. Background and source regions .....	60
Figure 17. Photo-absorbed NEI model on background-subtracted data .....	62
Figure 18. Photo-absorbed Pshock model fitted to blank sky background subtracted data .....	66
Figure 19. PN sky background .....	71

Figure 20. PN and MOS fit with sky background model .....	72
Figure 21. PN underfitting .....	74
Figure 22. PN data fit with absorbed Pshock model .....	75
Figure 23. Volume of selected region .....	79

## LIST OF SYMBOLS

$\text{\AA}$	Angstrom	unit of wavelength equal to $10^{-10}$ m
$\Theta$	Angular size	object's dimensions in degrees, arc minutes, and arc seconds
$k$	Boltzmann constant	$8.617 \times 10^{-5}$ eV K <sup>-1</sup>
eV	Electron volt	unit of energy equal to $1.602 \times 10^{-19}$ J
$S_0$	Integrated flux density	flux density measured over the entire remnant area, measured in Jy
$\tau$	Ionization timescale	quantifiable state of a remnants ionization
Jy	Jansky	flux unit equal to $10^{-26}$ w m <sup>-2</sup> Hz <sup>-1</sup>
$N_H$	Hydrogen column density	amount of material relative to hydrogen between the observer and the object
$h$	Planck's constant	$4.1357 \times 10^{-15}$ eV s
$kT$	Plasma temperature	describes energy of remnant particles; derived from spectral analysis
$n_e$	Post-shock electron number density	density of electrons upstream of the shock front
$z$	Redshift	displacement of spectral lines due to universal recession of galaxies
$\alpha$	Spectral index	power law exponent describing a spectrum
$c$	Speed of light	$3.0 \times 10^8$ m s <sup>-1</sup>
$\Sigma-D$	Surface brightness- diameter relation	antiquated distance determination (Green 1984)

## LIST OF ABBREVIATIONS

AGN	Active Galactic Nuclei
ARF	Ancillary Response File
CCF	Current Calibration File
CXB	Cosmic X-ray Background
FITS	Flexible Image Transport System
FWC	Filter Wheel Closed
GRXE	Galactic Ridge X-ray Emission
GTI	Good Time Intervals
HEASARC	High Energy Astrophysics
HEASoft	High Energy Astrophysics Software
MOST	Molonglo Observatory Synthesis Telescope
NEI	Non-Equilibrium Ionization
ODF	Observation Data File
Pshock	Plane-parallel shock
PPS	Pipeline Processing
PSF	Point Spread Function
RMF	Redistribution Matrix File
SAS	Science Analysis Software
SOC	Science Operations Centre
SSC	Survey Science Centre

## INTRODUCTION

The study of supernova remnants (SNRs) is only a couple of centuries old, and as expected for such a young science, researchers in the field have yet to learn many of the secrets locked within the physics of energetic explosions. Upon revealing these unknown details, we may decrypt some of the Universe's most complicated puzzles, including how the elements which make up our being came to gather in one location which we call our Solar System. To develop such knowledge, though, will require many large steps in the direction towards a complete understanding of supernovae and the processes which take place thereafter. Scientists are already in the midst of some of these pursuits; they are modeling the explosions using different stellar progenitors, observing existing supernovae, and much more. Observers of supernova remnants, in particular, aim much of their efforts at solving the mysteries that occur many years after a star has reached its end, not limiting themselves to how the ejected material behaves with the interstellar medium and which radiative processes take place as the remnant ages. These studies allow researchers to analyze one of the most energetic processes in the Universe; a feat which cannot be performed in any Earth-based laboratory. Their discoveries will shed light on current problems like heavy element formation and cosmic ray production, to name a few. Applicability of such knowledge encompasses several disciplines and so the value of supernova remnant research is limitless.

One topic of research, out of many, is the question of how the shape of SNRs evolves as the shock front propagates into the interstellar medium. As of now, computational modeling is only just scratching the surface of the complexity which describes the numerous parameters involved in such a process. The morphology, or shape, of the remnant may be affected by a number of factors like variation in the surrounding space, the inhomogeneous nature of the progenitor, etc. Observational astrophysicists, on the

other hand, have developed a way to side-step these complications by approaching this question in a reverse manner: studying the current remnant shape and working backwards. To solve more involved problems in morphological evolution, researchers look to remnants with more complex structures since those diverging from a spherical form tend to contain more information. But this wealth of knowledge comes with a price: typically investigating these remnants is much more difficult.

Our remnant, SNR G296.8-0.3, offers an opportunity to explore a complex morphology given that the remnant has displayed a very curious shape in both radio and infrared energies. In this thesis, we present the spectral examination of G296.8-0.3 in X-rays. A basic background of supernova remnants is provided; then we shift to the particulars of our object, including how we obtained and reduced the data. We then present our methods, followed by the resulting conclusions.

## A SUMMARY ON SUPERNOVA REMNANTS

Supernova remnants, or the remains of extremely energetic stellar explosions, continue to exist as astrophysical objects brimming with physical mystery. Details of the intricate processes which take place in SNRs successfully attract interdisciplinary scientists within the field of physics including nuclear, particle, computational, etc. The popularity of such research is justified by its numerous contributions to galactic evolution. The extreme amounts of energy produced in the formation of a SNR is rivaled by few other astrophysical events and hence makes an outstanding laboratory for high-energy physics such as shock formation and propagation, and its implications to interstellar media in the vicinity of the supernova. SNRs are also responsible to an extent for interstellar dust creation and destruction in addition to cosmic ray production. Perhaps one of the most interesting consequences of supernovae (SNe) is the production of elements heavier than iron. Hydrogen, helium, and trace amounts of elements slightly more massive than these were created during the early history of the Universe. Otherwise, all elemental nucleosynthesis takes place in stars and energetic processes like SNe (Moaz 2007).

Supernovae were first spectrographically studied in optical energies as early as 1885 (Branch 1990), or energies approximately ranging from 1 to 3.5 electron volts (eV), hence their historical classification is determined by specific properties seen in these energies. However, the confirmation that an object is in fact a supernova remnant takes place most commonly in radio wavelengths (less than a few meV). This scheme originated with the technological advances of the 1950s, especially with the operation of the NRAO Very Large Array. Researchers have developed the following criteria for the acceptance of SNR: first, the object must be relatively large in the plane of the sky, about  $.5^\circ$ ; second, the object should be polarized in radio energies, meaning the orientation of the electric fields of the detected photons must be highly correlated;

finally, when the information from radio observations is graphically displayed as the amount of incoming photons versus the energy of each photon, also known as a spectrum, the resulting curve must be non-thermal in origin (Reynolds 1998). Simply put, a non-thermal spectrum lacks any evidence of elemental line emission. Once an observer has noted these three qualities, a celestial object may be classified as a supernova remnant. Confirming the SNR's identity, though, is only the beginning of the investigation-- scientists are eager to know what the SNR was before the supernova, how it exploded, and what effects it has on its surroundings. To answer any of these questions requires an understanding of the stellar life cycle, which is presented in the next section. Knowing the theoretical origins of remnants allows researchers to limit the number of scenarios which lead to the evolutionary state of the remnant in question, thus providing the age, makeup, and type of remnant, as well as the structure and density of its surroundings.

## STELLAR ORIGINS

Progenitor stars, or stars which destruct into SNe, were once very similar to our Sun, in fact, they differed only in their masses. However, this difference is significant, for varying masses of stars result in different types of remnants. Low mass stars, or stars with less than 8 solar masses ( $8 M_{\odot}$ ), for example, have dissimilarly predicted outcomes than do stars with greater than  $8 M_{\odot}$ . Their beginnings, on the other hand are very similar: all stars spend the majority of their lives as main sequence stars where they maintain stellar equilibrium by balancing large gravitational pressures with fusion energy. Main sequence stars (see Fig. 1) convert hydrogen to helium in exothermic processes called p-p chain reactions or CNO cycles and release energy into the stellar environment. It is this outward pressure which balances with the inward forces of gravity. Eventually, though, a star's hydrogen supply will become depleted from the core, thus removing the pressure equilibration and causing gravitational forces to "squeeze" the star. This compression heightens the interior temperatures and ignites the core's helium as well as the outer layer of hydrogen (Schaaf 2008). At this time, the outer hydrogen envelope will expand, lowering the star's effective temperature while the core's contraction increases its stellar luminosity. In Fig. 1, this is represented by moving a main sequence star to the right and up, hence the star becomes a red giant.

The time a star spends on the so-called "giant branch" is relatively short lived, lasting only a tenth of the star's time on the main sequence branch. As a red giant, the star experiences heavy mass loss in its outer regions since the low density particles are only loosely bound to the star. Meanwhile, the core's helium is being converted to carbon and oxygen through triple-alpha reactions, or reactions using helium nuclei to create carbon or oxygen. It is at this stage that the core of a low mass star will reach a dense equilibrium state in which electron degeneracy pressure counteracts gravitational collapse, thus preventing the creation of

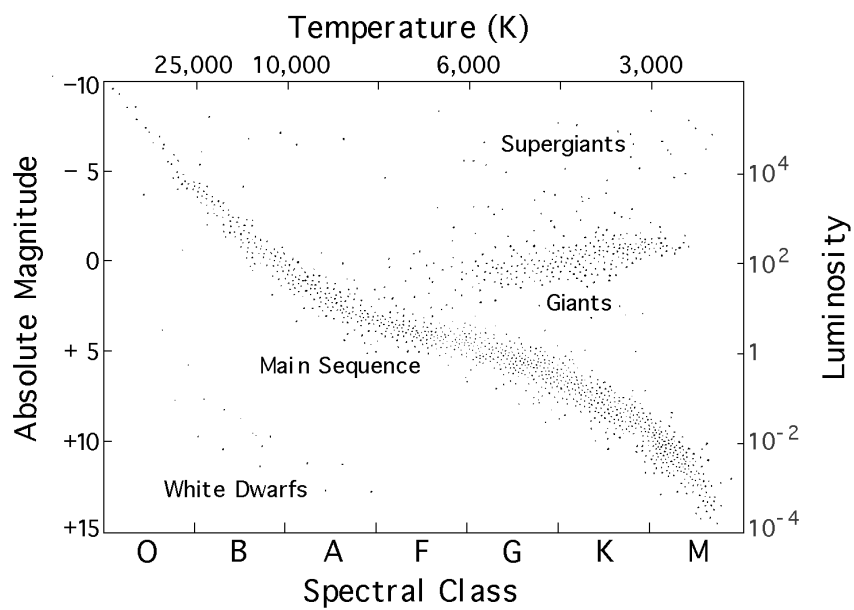


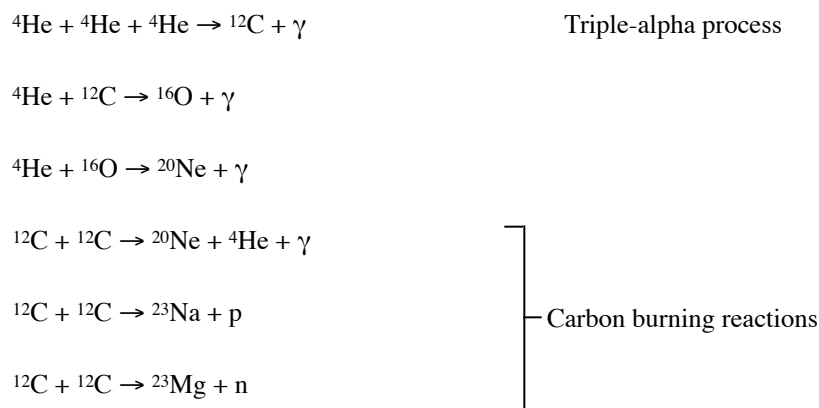
**Figure 1.** Hertzsprung-Russell diagram. The H-R diagram logarithmically represents the absolute magnitude and luminosity of stars as a function of decreasing temperature. Stellar evolution is spent predominantly in the main sequence branch, then precedes to other branches. *Image courtesy of NASA.*

elements heavier than oxygen. The resulting star is very compact and hot; because of its small radius, the luminosity will drop several orders of magnitude from its value as a red giant. Simultaneously, the temperature increases dramatically. Hence, the star's position on the Hertzsprung-Russell diagram, beginning on the giant branch, moves down and to the left into the white dwarf region. Outside the core, the outer gaseous envelope may be energetically ejected creating a planetary nebula and leaving behind a small carbon-oxygen white dwarf star. If left unperturbed in space the dense white dwarf, a star with a radius comparable to Earth's and a mass comparable to the sun's, has reached its ultimate evolution (Moaz 2007).

When a white dwarf is in close proximity to a more massive star, the binary star system has the potential to become a supernova. If the star accompanying the white dwarf, called the companion star, is close enough in distance, the white dwarf's gravity will begin accreting the companion star's outer layers onto itself. As the two stars orbit one another, that material cannot fall directly onto the white dwarf because of its angular momentum. Instead, it swirls in and forms an "accretion disk." As the system evolves, the white dwarf may in time reach a critical mass of  $1.4 M_{\odot}$ , called the Chandrasekhar mass, where the star can no longer be supported by electron degenerate pressure. At this point, the core reignites into a runaway fusion process, ultimately exploding as a supernova releasing  $\sim 10^{51}$  ergs of energy, or  $\sim 6 \times 10^{59}$  keV. For comparison, this is more energy than the sun has produced in its entire lifetime (Williams 2004)! A white dwarf supernova, also called a thermonuclear or Type Ia supernova, leaves no stellar remnant.

The evolution of the progenitor for a different type of supernova, called a core collapse SN, progresses much differently than a thermonuclear one. If a star is considered a high mass star, in other words it has greater than  $8 - 10 M_{\odot}$ , its life will progress much differently than that of a star with mass comparable to our Sun's. Just as in low mass stars, a high mass star initially fuses hydrogen into helium in exothermic reactions. Eventually, the core of a high mass star will undergo elemental burning similar to the red giant star

discussed above. Again, the star's outer hydrogen envelope will expand significantly; particles in these low-gravity regions create a fast stellar wind which modify the surrounding interstellar medium. Astrophysicists refer to interstellar material disturbed by a star's ejecta as circumstellar material (CSM). Unlike low mass progenitors, the gravity of high mass stars provides considerably more energy, causing the core-burning to create progressively heavier elements through fusion processes. This nucleosynthetic burning front advances radially outward creating layers of elemental ash, shown in Fig. 2. The progression of the innermost layer is as follows: hydrogen atoms are fused into helium by p-p chain reactions, then helium is fused into carbon and oxygen by the triple-alpha process. Carbon burning then creates  $^{20}\text{Ne}$ ,  $^4\text{He}$ ,  $^{23}\text{Na}$ , and  $^{23}\text{Mg}$  in addition to photons, protons, and neutrons (the superscript immediately before the element name is the mass number,  $A$ , or sum of protons and neutrons, in an atom). The exact reactions are below for reference:



Carbon burning precedes neon, oxygen, and silicon burning. By continuing these exothermic reactions, the innermost layer of the core will inevitably reach the iron group elements, or those elements with atomic number, or number of protons, ranging from 24 to 28, including chromium, manganese, iron, cobalt and

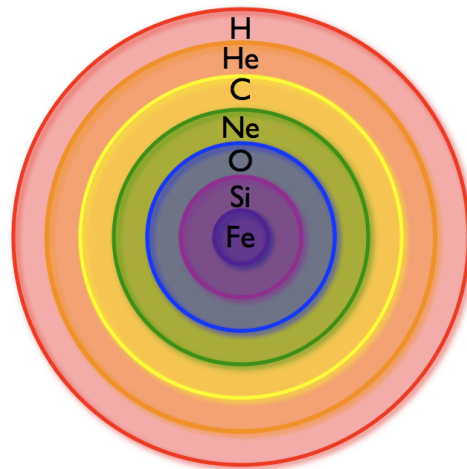


**Figure 2.** Burning stages of a core collapse progenitor. High mass stars undergo nucleosynthesis in onion-like layers.

nickel (Moaz 2007), see Fig. 3. The production of these elements and those with higher atomic numbers, however, is an endothermic process, meaning energy is consumed rather than emitted. In response, the core will compress to a state in which it is being supported solely by electrons, or by electron degeneracy pressure. The opposing electron degeneracy pressure and gravitational potential energy are highly unstable, and will eventually break down causing further collapse. The outer layers of material will fall radially inward with a velocity that increases with radius. However, the speed of sound behaves oppositely due to the steepening density as the matter approaches the electron-rich core. The resulting effect is a subsonic, infalling core and a supersonic blast wave of material speeding towards the star's dense interior. The lighter, fast-moving particles in the surface region will "bounce" off the dense core and be propelled into space at high energies. Densities in the core continue to grow until they are comparable to that of nuclear matter, forming an incompressible core. This discontinuity between the supersonic outer layers rebounding off the core, and surrounding material, becomes the shock wave which is ultimately responsible for stellar disruption (Mezzacappa 2005).

The energy produced during a core collapse supernova is approximately  $10^{53}$  ergs,  $10^{51}$  ergs of which is kinetic energy. The remaining energy is carried off by neutrinos, or extremely low-mass subatomic particles produced as the shock propagates outward through the edges of the core and into the remaining outer layers. A proto-neutron star is now formed consisting of a cooler, unshocked interior and a hot, fluid surface. During the subsequent explosion, though, the proto-neutron star will either become a neutron star, an extremely dense, rapidly rotating star with an immense magnetic field, or a black hole, depending on the extent of the disruption (Mezzacappa 2005). The final core collapse product is a compact object--a neutron star or black hole--encircled by high-velocity, radially projected stellar ejecta. Neutron stars may possess

hydrogen 1 H 1.0079	helium 2 He 4.0026																
lithium 3 Li 6.941	beryllium 4 Be 9.0122											boron 5 B 10.811	carbon 6 C 12.011	nitrogen 7 N 14.007	oxygen 8 O 15.999	fluorine 9 F 18.998	neon 10 Ne 20.180
sodium 11 Na 22.990	magnesium 12 Mg 24.305											aluminum 13 Al 26.982	silicon 14 Si 28.086	phosphorus 15 P 30.974	sulfur 16 S 32.065	chlorine 17 Cl 35.453	argon 18 Ar 39.948
potassium 19 K 39.098	calcium 20 Ca 40.078	scandium 21 Sc 44.956	titanium 22 Ti 47.867	vanadium 23 V 50.942	chromium 24 Cr 51.996	manganese 25 Mn 54.938	iron 26 Fe 55.845	cobalt 27 Co 58.933	nickel 28 Ni 58.693	copper 29 Cu 63.546	zinc 30 Zn 65.39	gallium 31 Ga 69.723	germanium 32 Ge 72.64	arsenic 33 As 74.922	selenium 34 Se 78.96	bromine 35 Br 79.904	krypton 36 Kr 83.80
rubidium 37 Rb 85.468	strontium 38 Sr 87.62	yttrium 39 Y 88.906	zirconium 40 Zr 91.224	niobium 41 Nb 92.906	molybdenum 42 Mo 95.94	technetium 43 Tc [98]	ruthenium 44 Ru 101.07	rhodium 45 Rh 102.91	palladium 46 Pd 106.42	silver 47 Ag 107.87	cadmium 48 Cd 112.41	indium 49 In 114.82	tin 50 Sn 118.71	antimony 51 Sb 121.76	tellurium 52 Te 127.60	iodine 53 I 126.90	xenon 54 Xe 131.29
cesium 55 Cs 132.91	barium 56 Ba 137.33	lanthanum 57-70 * [57-70]	hafnium 71 Hf 178.49	tantalum 72 Ta 180.95	tungsten 73 W 183.84	rhenium 74 Re 186.21	osmium 75 Os 190.23	iridium 76 Ir 192.22	platinum 77 Pt 195.08	gold 78 Au 196.97	mercury 79 Hg 200.59	thallium 80 Tl 204.38	lead 81 Pb 207.2	bismuth 82 Bi 208.98	polonium 83 Po [209]	astatine 84 At [210]	radon 85 Rn [222]
francium 87 Fr [223]	radium 88 Ra [226]	actinide series 89-102 * * * [89-102]	actinium 89 Ac [227]	thorium 90 Th 232.04	protactinium 91 Pa 231.04	uranium 92 U 238.03	neptunium 93 Np [237]	plutonium 94 Pu [244]	americium 95 Am [243]	curium 96 Cm [247]	berkelium 97 Bk [247]	californium 98 Cf [251]	einsteinium 99 Es [252]	fermium 100 Fm [257]	mendelevium 101 Md [258]	nobelium 102 No [259]	unnilquadium 114 Uuq [284]

* Lanthanide series													
lanthanum 57 La 138.91	cerium 58 Ce 140.12	praseodymium 59 Pr 140.91	neodymium 60 Nd 144.24	promethium 61 Pm [145]	samarium 62 Sm 150.36	europium 63 Eu 151.96	gadolinium 64 Gd 157.25	terbium 65 Tb 158.93	dysprosium 66 Dy 162.50	holmium 67 Ho 164.93	erbium 68 Er 167.26	thulium 69 Tm 168.93	ytterbium 70 Yb 173.04
** Actinide series													
actinium 89 Ac [227]	thorium 90 Th 232.04	protactinium 91 Pa 231.04	uranium 92 U 238.03	neptunium 93 Np [237]	plutonium 94 Pu [244]	americium 95 Am [243]	curium 96 Cm [247]	berkelium 97 Bk [247]	californium 98 Cf [251]	einsteinium 99 Es [252]	fermium 100 Fm [257]	mendelevium 101 Md [258]	nobelium 102 No [259]

**Figure 3.** Periodic table of elements. A visual representation of the elements created in supernovae. The atomic number,  $Z$ , is given just below the element name. *Image courtesy of BPC-Department of chemistry.*

intense magnetic fields and rapid rotation, the combination of which projects an energetic beam of radiation into interstellar space. When an observer's line of sight intersects this beam, the misalignment of the rotational axis and the magnetic field axis cause a lighthouse-like effect, and the beam is visible once during each rotation in pulses. This particular type of neutron star is aptly termed a pulsar (Lochner, 2010). The magnetic field of the pulsar is responsible for trapping some ejecta particles, preventing them from traveling with the shocked ejecta. These particles give off radiation, allowing researchers to study the behavior of the pulsar's complicated magnetosphere.

An important difference between CC SNe and Type Ia SNe is the modification of the interstellar medium. A core collapse progenitor spends much more time in the giant phase, and thus releases more of its outer layers into the surrounding media than do thermonuclear progenitors. Because the supernova of a high mass star occurs shortly after, or in some cases *during* the stellar wind phase, the SN ejecta will interact with circumstellar material, and thus modify the morphology of CC SNe. Interactions of this sort are not expected in Type Ia SNe as the progenitor's stellar wind has thoroughly dissipated in the time taken to undergo accretion to Chandrasekhar mass. Therefore by examining a SN or SNR for evidence of disturbed interstellar media, one may find clues as to the type of progenitor star.

## SNe TYPOLOGY

SN spectral studies are still very young--the oldest known report was published just over 100 years ago. Within any scientific field, preliminary matters such as nomenclature and classification will continue to be modified as long as new discoveries are made. Just as the lines between remnant morphologies are blurred, so are their typologies. Types of SNe are historically defined by their spectra during maximum light (immediately after the supernova) and late-times (about six months after the SN) (Harkness and Wheeler 1990) when the SN has become optically thin. Spectra during maximum-light and late-times differ greatly. Directly after the explosion, the light curve of the SN reaches a maximum and the ejected materials' spectra appear similar to expanding stellar photospheres dominated by elemental absorption. A couple of months after maximum brightness, the optical opacity of this "stellar envelope" dims, and becomes transparent to continuum photons, or photons which create the body of the spectrum minus elemental emission and absorption lines. At this time, the ejecta has become a "self-excited nebula" and emission lines dominate the spectrum, allowing insight into the SN's nucleosynthetic processes (Branch 1990).

Elemental differences between late-time SN spectra constitute the type of supernova. This naming convention was first proposed by Minkowski, who grouped SNe according to the presence or absence of hydrogen features: Type II if the spectrum showed hydrogen; Type I if not (1939, 1940). Since then, Type I and II have been divided into subclasses and additional categories have been suggested, including a Type V by early remnant scientist Fritz Zwicky who aimed to classify SNe with uniquely narrow hydrogen absorption lines (Harkness and Wheeler 1990). However, most of these motions have been denied by the scientific community because each SN spectrum is different, and classifications of all such variations would lead to systematic complications.

As previously stated, Type I spectra have no hydrogen (H) lines. Currently, three subclasses of Type I supernovae (SN I) exist: Type Ia, Type Ib, and Type Ic. The former of these, Type Ia, lack helium (He) in addition to H, and show strong Si features, specifically Si II  $\lambda$ 6150. (As an aside, to interpret spectra one should be familiar with atomic notation. The “II” in Si II means the neutral Si atom having 14 electrons, has had one electron stripped from its energy levels. Neutral Si is written Si I. The trailing “ $\lambda$ 6150” denotes the wavelength of the spectral line created by Si II in angstroms (Å)). Another subclass, Type Ib, does not lack He as SN Ia do; they show sharp He features, like He I  $\lambda$ 5878 (Harkness and Wheeler 1990). Finally, H, He, and Si are absent in Type Ic spectra (Wheeler and Harkness 1986). Complicating what appears to be a simple system, the spectra of the late-time SNe vary greatly from the maximum-light spectra, which were just described. Within a couple of months, many prominent features arise in Type I supernovae. SN Ia show overlapping emission lines of [Fe II], [Fe III], and likely [Co III] with Ca II absorption and no real evidence of oxygen (brackets denote a “forbidden” transition, meaning it has a much lower probability of occurring than non-forbidden ones) (Harkness and Wheeler 1990). Conversely, late-time SN Ib show strong [O I]  $\lambda$ 6300, 6364 accompanied by Ca and Mg I  $\lambda$ 4562 (Axelrod 1980). The similarities of SN Ib and SN Ic are theorized to arise from a common progenitor system, but may differ simply by He-rich and He-poor envelopes (Harkness and Wheeler 1990). This matter is still the subject of much research.

The thermonuclear origins of SN Ia, however, are greatly supported in the field. Recall thermonuclear SNe are created from accreting white dwarf systems. In fact, the late-time emergence of iron and cobalt described above are attributed to the radioactive decay of nickel formed during the deflagration of the carbon-oxygen white dwarf (Moaz 2007). These types may be differentiated from core collapse events by examining their light curves, or their luminosities plotted as functions of time. A Type Ia light curve has a much sharper maximum when compared to core collapse events. As a rule, the peak absolute magnitudes of

SN Ia are very constant, perhaps due to mass similarities of the progenitor stars when they reach the Chandrasekhar limit. Because of this consistency, SN Ia may be used to calculate distances by comparing their known luminosity to apparent brightness.

The hydrogen-possessing remnant, better known as a Type II SN, has core collapse progenitors which expel at least 8 solar masses of ejecta. The progenitors are massive and may be red supergiant stars or even stars with greater than 25 solar masses and extremely energetic stellar winds called Wolf-Rayet stars (Chevalier 1990). At late-times, the spectra of H-rich SN II show Balmer line emission (Harkness and Wheeler 1990). There have been several proposed subclasses of Type II supernovae based on the shape of their light curve after maximum brightness, including Type II-L, which show a linear drop in radiation and Type II-P describing light curves with a plateau after maximum (Barbon et al. 1973). Another subclass, Type IIn, was proposed by Schlegel (1990), to describe SNe light curves with narrow emission lines likely due to the surrounding H II regions.

## SNR EVOLUTION

All that is left of the SN--including hot ions streaming away from their stellar origin, the resulting neutron star or black hole, and the surrounding circumstellar (CSM) and/or interstellar medium (ISM)--constitutes what is known as a supernova remnant. Studying a SNR's shape, called its morphology, reveals several aspects of its evolution, such as how the ejected stellar material expanded throughout the CSM and/or ISM and the uniformity of such media. (For the remaining explanations, although it is understood the material surrounding a SN can be either circumstellar or interstellar, *any* material circumscribing the SN will be referred to as interstellar material.) Before one may interpret a SNR's morphology, he or she must be familiar with the progression of a supernova's ejecta after the initial explosion. Some researchers have attempted to label the stages of a remnant's evolution by analyzing the mass and velocity of the ejecta and grouping similar properties into one phase. However, a rigid criterion has yet to be officially accepted by the scientific community because the entire progression is nonlinear. In other words, there is no one set of evolutionary phases which exactly describes all SNRs. Not to mention several aspects, not limited to magnetic field contributions and simultaneous density variations, have yet to be applied to the existing schematic (Reynolds 1988). Below is an elementary outline generally describing SNR development.

*Anatomy of a supernova remnant:* Once the white dwarf has reached the Chandrasekhar mass, or in the case of core collapse supernovae, the core has reached neutron degeneracy pressure and the surrounding mass has forcefully blasted away from the dense interior, the ejecta, or the mass formerly comprising the star, travels at a velocity much faster than the speed of sound in the ISM, forming a shock wave. Immediately behind the shock front a surface called the

contact discontinuity separates the shocked ejecta from the shocked interstellar medium, see Fig. 4. The interactions occurring here are not simply the result of particles elastically colliding with one another, called a Coulomb collision. The density of interstellar space is so sparse a collision of this sort is highly unlikely. Instead, the charged particles gyrate in a magnetic field and the effective mean free path is on the scale of the resulting gyroradius, or the radius of circular motion attributed to charged particles in a magnetic field. Thus interactions are collisionless. Particles traversing the Earth's bow shock undergo the same interactions (Reynolds 1988). As the shock front progresses further away from its origin, an increasing amount of ambient medium is swept up and carried behind the blast wave.

*Free Expansion:* The ejecta of a supernova remnant is blasted away from the location of the progenitor with  $10^{51}$  ergs of energy, causing illumination in visible light anywhere from weeks to months, depending on the distance from Earth. However, the true free expansion phase may be measured in units of days. During this phase, the shocked ejecta propagates through the surrounding ISM with velocities of 5,000 to 10,000 km s<sup>-1</sup> with no deceleration as the forward motion of the shock is uninhibited by the accumulating mass of the swept-up ambient medium (Dyer 2001). Thus the pressure across the contact discontinuity is constant, clearly separating the ejecta from the shocked ISM (Reynolds 1988). As long as the SN does not lose large amounts of energy due to accelerating particles to relativistic velocities, the kinetic energy partitioned to fueling the movement of the shock is now being converted directly into thermal energy and the entire system maintains an energetically conservative nature--meaning thermal energy neither enters nor leaves the system, hence it is adiabatic (Reynolds 2008).

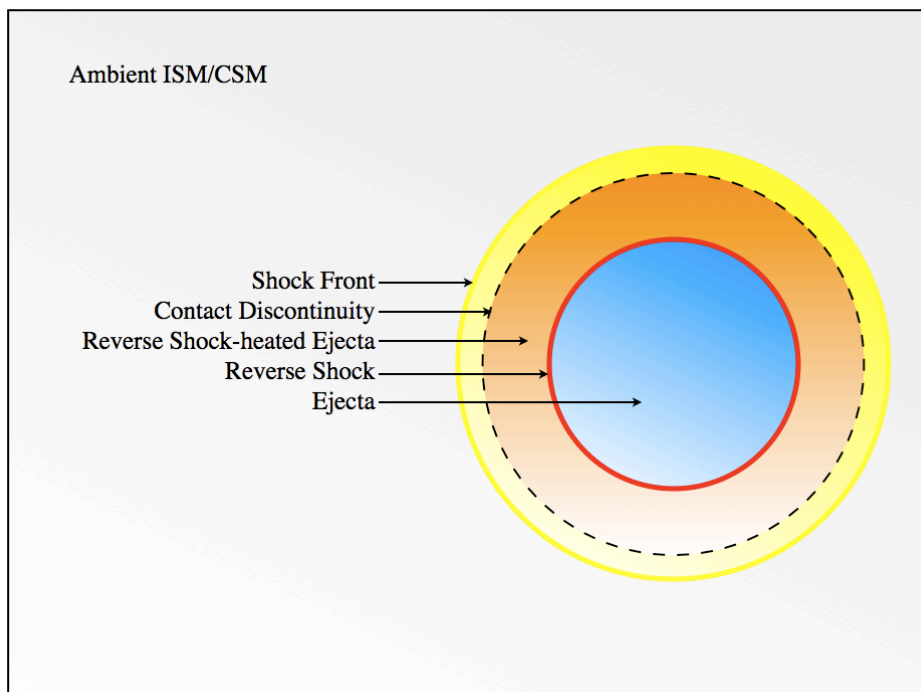


**Figure 4.** The anatomy of a supernova remnant. Above is a simplified representation of a supernova remnant with each of the features labelled. Not all remnants possess each of the components shown.

*Ejecta Driven Phase:* Directly following the short-lived free expansion phase, the SN's blast wave has swept up enough mass to begin deceleration. As the shock front slows, particles further inside the blast wave begin plowing into the slower particles near the outer edge, forming a reverse shock facing inwards reheating the ejecta, see Fig. 4. At first, the velocity of the reverse shock is very slow and energy is rapidly radiated away, but in very little time the shock velocity can reach the X-ray emitting threshold. In a spherically symmetric approximation, the expansion may be self-similar: plots of density, temperature, and pressure inside the remnant maintain the same shape as it evolves. Also, the adiabatic nature of the free expansion phase persists into this stage of evolution, which may last hundreds to thousands of years depending on the density and structure of the ISM. By the end of the remnant's lifetime, the reverse shock will have propagated back to the center of the remnant and disappeared (Reynolds 2008).

*Sedov Phase:* The next phase begins when the swept up mass becomes greater than the ejected mass. The momentum of the shock front is still very strong despite its deceleration under the weight of the collected ISM. One may now use Sedov dynamics to quantify the parameters of the SN, like age, explosion energy, and ambient density. See Reynolds 2008 for detailed formulae. The Sedov phase ends when the adiabatic approximation fails due to significant deceleration of the shock front.

*Radiative Phase:* The subsequent stage of a SNR's evolution occurs when the shock front has slowed tremendously as the swept-up mass has greatly surpassed the ejecta mass. This period

is aptly named the radiative phase because the age of the remnant is now comparable to cooling timescales of gas and much of the energy is being radiated away as the adiabatic nature of the supernova no longer exists. A loss of half the initial thermal energy approximately indicates the onset of the radiative phase. In addition, the magnetic field becomes increasingly important as the ambient materials to which it is frozen have undergone extreme compression near the blast wave (Reynolds 2008).

*Dissipation Phase:* The finale of a SNR takes place during the dissipation phase, also called the merging phase. The once energetic particles have now cooled and equilibrated to the temperature of the surrounding ambient material. At this point, all particle velocities have become subsonic and propagate into the ISM as sound waves. After a million or so years, even this evidence of one of the most energetic explosions known to the universe will disappear completely (Reynolds 1998). However, the contributions from the SN live long after its remains have faded; the newly formed heavy elements and dust may recombine creating new, metal-rich solar systems like our own.

## SNR MORPHOLOGY

Three general SNR morphologies are agreed upon among the physics community and are categorized according their appearance in radio energies: shell-like, Crab-like, and composite (Rho and Petre 1998). An ideal shell SNR is formed by allowing SN ejecta to uniformly expand into isotropic media; this produces a purely spherical shock front. A SNR of this sort will experience limb brightening, a consequence of “looking through” more of the SNR around the edges, see Fig. 5, creating a shell-like illusion. Naturally, the ideal circumstance never exists due to common inhomogeneities arising from nonuniform stellar material and density differences in the ISM. Observations of shell-like SNR reveal limb-brightened structures; how complete the shell appears is determined by the aforementioned parameters. Tycho’s SNR, the result of a SN in 1572 studied by Tycho Brahe, is a good example of a shell SNR, see Fig. 6. According to early assessments by Baade and Zwicky, Tycho’s SNR shows properties of the thermonuclear classification, including the absence of an interior compact object (Marschall 1988). Regardless, both thermonuclear and core collapse supernova may develop into a shell SNR. Crab-like supernova remnants, on the other hand, are restricted to core collapse (CC) supernovae only. This class of SNR are also called “plerionic” because they possess a plerion, or a nebula of material believed to be fueled by the interior pulsar (Manchester 1994), although often there is no direct evidence of the pulsar itself (Slane et al. 2000). They are characterized by their lack of shell and their center-filled appearance in radio energies, in addition to displaying more polarization than other morphologies. Crab-like remnants are named after the Crab Nebula, a well-studied plerionic SNR which demonstrates the ideal properties of a Crab-like remnant, see Fig. 7.

The third type of supernova remnant, composites, are simply a mixture of the two morphologies previously described: plerionic and shell-like (Rho and Petre 1998). Furthermore, other composite

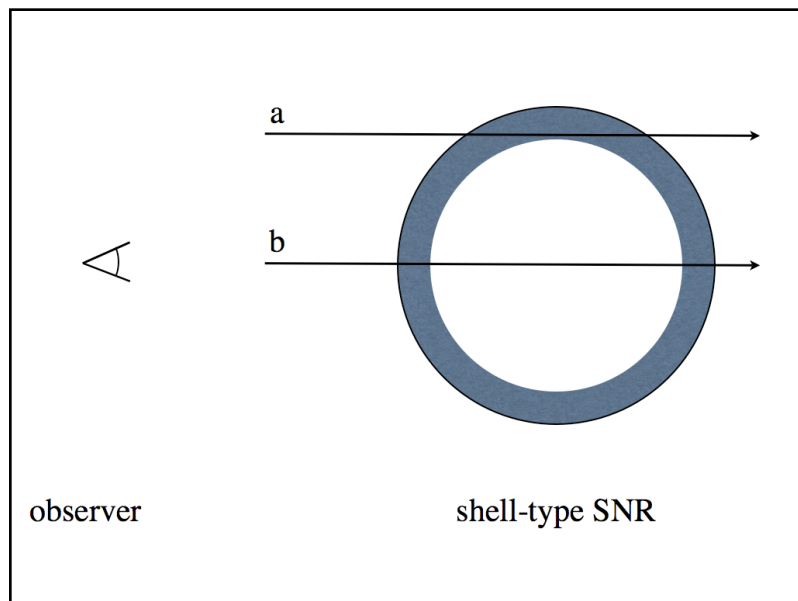


**Figure 5.** Limb brightening. In a shell-type SNR, most of the mass is directly behind the shock front. An observer a great distance away receives light in parallel rays. Clearly, there is more material along the line of sight when looking through *a*) the edge of the the SNR as opposed to *b*) the center; thus the edges appear brighter than the interior, giving the illusion of a “shell.”

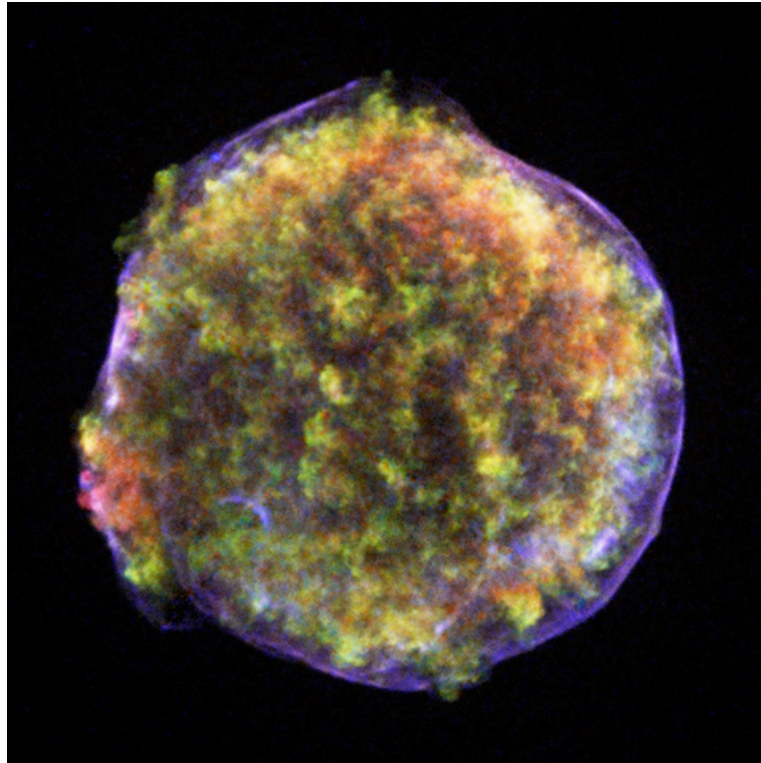


**Figure 6.** Tycho's supernova remnant. Tycho's supernova remnant, observed here by the *Chandra* X-ray Observatory, is a good example of shell-like morphology. Colors indicate X-ray energies. Notice the limb brightening in the region of the forward shock (*blue*). The center illumination (*red and green*) is from the reverse shocked material. *Image courtesy of NASA.*

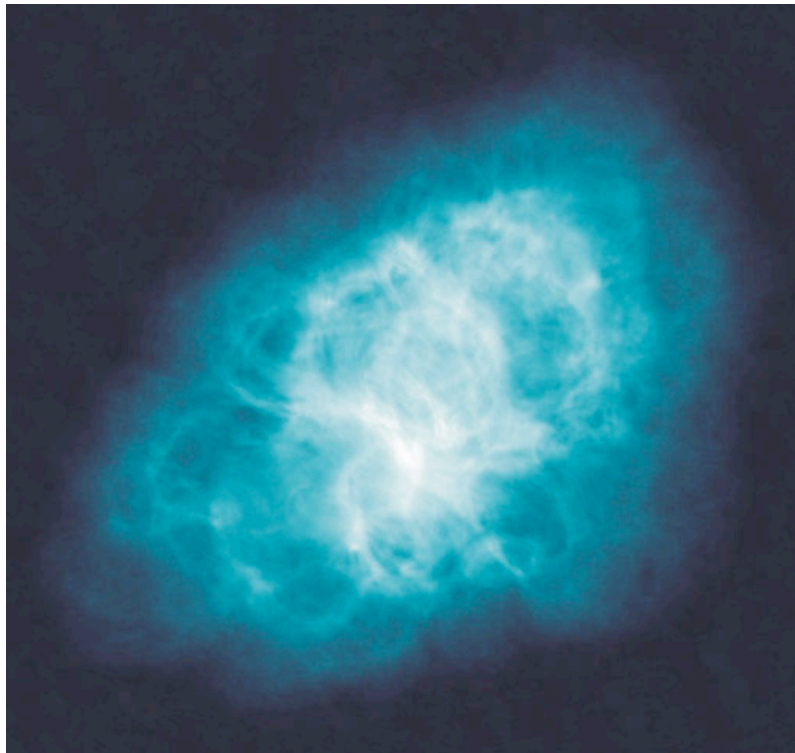


**Figure 7.** The Crab Nebula in radio energies. Crab-like SNR are named so because of this nebula, the Crab Nebula. This image was taken by the NRAO Very Large Array (VLA). The center-filled region is illuminated by electrons trapped in the pulsars large magnetic field. *Image courtesy of NASA.*

morphologies have been proposed to facilitate classifications showing different features in different energy bands. For instance, Rho and Petre suggested a mixed-morphology remnant (MM) to accommodate remnants with radio-bright shells and X-ray bright, but thermal, centers (1998). Jones et al. calls this class thermal X-ray composites, or TXCs (1998). While the nomenclature for this latest class of SNR remains unclear, researchers have dedicated much time to exploring their formation, the scope of which is beyond this thesis.

## SNRS IN MULTIPLE WAVELENGTHS

Already, some of the benefits of observing remnants in different energy bands are apparent, like the visibility of core components including the shell and pulsar via radio and X-ray energies and the appearance of elemental emission features in optical and infrared. Having the ability to observe an object in several wavelengths applies useful constraints to the amount of parameters used to deduce the physical processes taking place in the remnant. Two significant ways to analyze data taken from supernova remnants exist: imaging and spectroscopy. When one images a supernova remnant, he or she is plotting the location of detected photons on a grid representing the  $x$ - and  $y$ - axes of the detector. This sounds complicated, but it is nearly the same process one uses to see optical light--only in that case the eye is the detector. Imaging gives instant clues to the origin and properties of remnants including angular dimensions and the homogenous nature of the ISM. In some cases, a compact object is visible, as in the Crab Nebula, see Fig. 8b.

Spectroscopy, on the other hand, investigates much more quantifiable characteristics in remnants. When a spectrum is generated, one is able to conclude specific radiation and emission properties, such as the emission flux and ionization state. Observing an object in more than one energy band provides a better history of the remnant. For example, a comparison of Fig. 7 and Fig. 8 demonstrates the variation in the Crab Nebula in four different energy bands: radio, infrared, optical, and X-ray. The Crab Nebula in radio energies (Fig. 7) displays a cloud of material that was likely blown out by the pulsar during its formation and subsequently trapped in its strong magnetic field. Fig. 8a shows the same object but in infrared energies. Spectral analyses have verified that the blue-white radiation shown in this image is non-thermal synchrotron radiation (Smith 2008). The X-ray radiation displayed in Fig. 8b, reveals the locations of hot, highly ionized atoms caught in the equatorial winds of the pulsar. Finally the optical image (Fig. 8c) reveals strange

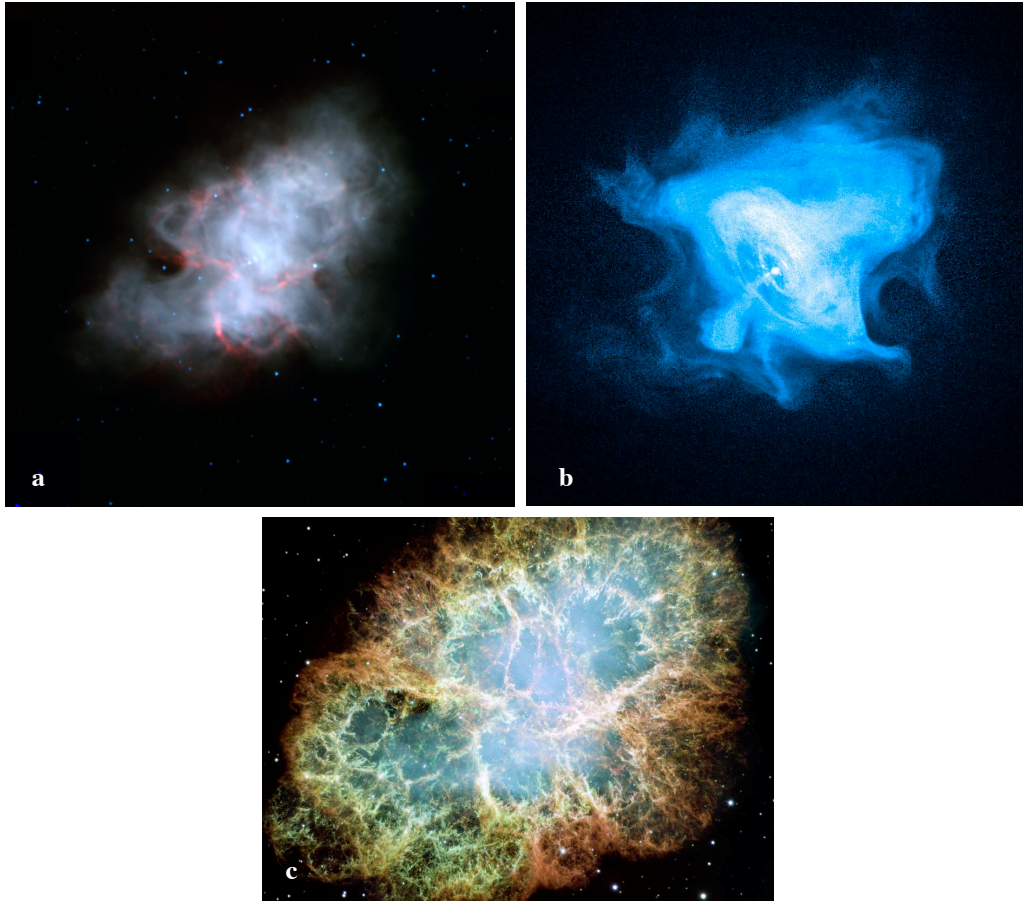


**Figure 8.** The Crab Nebula in infrared, X-ray, and optical energies. *a)* Taken by the Spitzer Space Telescope, this image displays the synchrotron radiation as a blue-white cloud caused by the interior rotating pulsar (Smith 2008) *Image courtesy of NASA/JPL-Caltech/R. Gehrz.* *b)* A close up of the pulsar's equatorial winds; observed by the Chandra X-ray Observatory. *Image courtesy of NASA.* *c)* Mysterious filaments observed from Hubble's optical telescope. Mass calculated from this image is much less than the theoretical progenitor mass. *Image courtesy of NASA/ESA/J.Hester, A. Loll*

filaments of the progenitor's material. When combining the information from these four observations, much more detail concerning the evolution of the Crab Nebula may be formulated.

Many different physical processes may cause SNRs to radiate in specific energies. Typically, observation of radiation is limited to certain wavelengths because the physics taking place to produce these energetic photons is restricted to a certain bandwidth. Because research included in this thesis takes place in X-rays, the following explanations will be limited to these energies.

## X-RAY EMISSION IN SNRS

X-rays are the second most energetic classification of electromagnetic radiation, preceded only by gamma-rays. Wavelengths of X-rays range from approximately 0.1 to 10 nm, corresponding to energies of .1 to 125 keV. There are several radiative processes by which SNRs emit X-rays, specifically thermal and non-thermal processes, to be explained soon. When stellar material is ejected in the supernova, the velocities of the particles exceed several thousand kilometers per second. These extremely energetic particles in the shell of SNRs, consisting of ions and free electrons, form a plasma and travel radially outward towards the ambient interstellar medium with very high velocities. Often, they will come within the cross-sectional area of other fast-moving particles as well as relatively slow particles in the ISM. If a free electron approaches an ion, for instance, the electric field of the two oppositely charged particles will cause the less-massive electron to slow and curve away from the ion, emitting a photon during the deceleration. This type of radiation is appropriately called Bremsstrahlung, meaning “braking radiation” in German. The emitted photon has an energy comparable to the energy of the electron which emitted it, and recalling the high velocity of the particles (and thus high energies), the emitted photon may very well be of X-ray energies. When there are many electrons in an environment favorable for Bremsstrahlung radiation, as is the case of the cloud of SNR ejecta, many photons will be emitted at similar wavelengths, shaping what is known as the continuum of a remnant’s spectrum. The energy of these photons, and hence the velocities, closely determines the temperature of the environment which produced them (Culhane and Sanford 1981).

Bremsstrahlung radiation, or free-free radiation, is only one type of thermal radiation; bound-bound, free-bound, and bound-free radiations exist as well. A thermal process simply means the velocities of particles are in a thermal, or Maxwellian, distribution. Furthermore, the names “bound” and “free” are

chosen to specify the condition of the particle before and after photon emission and/or absorption has taken place. In the case of an electron undergoing Bremsstrahlung radiation, for example, the electron is in a free state, emits a photon, then continues its journey as a free particle, hence the label “free-free.” Free-bound radiation occurs when a free electron is captured by an atom, emits a photon and settles into a previously unoccupied energy level of the atom (Dyer 2001). The spectral distribution of free-bound radiation is similar to the continuum produced by Bremsstrahlung radiation except for the presence of so-called “edges.” The energy of the atomic shell in which the captured electron now resides determines the placement of such edges. Another sort of radiation termed bound-free radiation, or photoionization, is produced when a bound electron absorbs a photon with enough energy to free it from the atom. However, the probability of photoionization lessens with decreasing photon energy *but* increases with the atomic number of the atom (Culhane and Sanford 1981). Therefore, a highly energetic photon, like those in SNR ejecta and in the swept up ISM, will have a greater chance of transferring its energy to electrons in partially ionized atoms rather than to hydrogen-like and helium-like atoms, having only one or two bound electrons, respectively.

The last category of thermal emission is called bound-bound radiation, a process particularly important because it traces elemental abundances in the remnant via line emission. In bound-bound radiation, a photon is absorbed by an electron, sending it to a higher energy shell where it remains for a very short time. The electron then emits a photon having the same energy as the absorbed one, then returns to its previous ground state. Differencing the energies of the excited state and ground state of the electron gives the emission energy of the photon,  $\Delta E$ . Because the energies of emitted photons are very specific to the energy shells of the atom containing the electron, one may deduce which element is emitting by comparing  $\Delta E$  to known line emission energies. Furthermore, because particles in the remnant’s shell are in thermal equilibrium, one would expect only transitions in a specific energy range corresponding to the plasma

temperature to take place (Culhane and Sanford 1981). Thus, the line emissions are restricted by the temperature of the plasma and so one may derive this temperature from the types of abundances in the spectra, and vice versa. Note here that a very hot, shocked material will have heavily undergone bound-free radiation, leaving most of the atoms with only a few electrons, lessening the chances of photon absorption.

For completeness, non-thermal radiative processes may take place in supernova remnants at X-ray energies, albeit somewhat unlikely. Non-thermal X-ray emission is simply emission produced by a non-Maxwellian distribution of electron velocities. Synchrotron radiation is a form of non-thermal radiation in which electrons begin to spiral around magnetic field lines, emitting photons due to their changing centripetal acceleration. The energy of the photon now corresponds to the strength of the magnetic field as well as the electron energy. For the most part, synchrotron radiation takes place in two major regions: in the presence of a pulsar's extended magnetic field creating synchrotron radiation at radio energies, and in the swept up medium outside the shock front producing high-energy cosmic rays. In the latter case, the magnetic field of the ambient interstellar medium is also carried and compressed by the shock front. The compression results in an amplified magnetic field able to accelerate electrons and ions to gamma-ray energies, thus producing cosmic ray particles. While synchrotron radiation has been observed in X-rays (see Borkowski et al. 2001), their detection remains elusive in most remnants, save a few young ones.

## XMM-NEWTON AND SAS

The instrument used to perform X-ray observations of G296.8-0.3 is the European Space Agency's X-ray telescope, *XMM-Newton*. This space based observatory houses an X-ray telescope focused onto three X-ray CCD cameras, collectively called EPIC, or European Photon Imaging Cameras. Possessing a field of view (FOV) of 30 arc minutes and a spectral resolution of  $E/\Delta E \sim 20-50$  from  $\sim 2$  to 14 keV, EPIC is ideal for studying extended sources with low surface brightness. The CCDs are not of the same type, instead *XMM-Newton* accommodates one detector called PN and two others called MOS, named for their detector properties. The PN uses p-n junctions and is completely unobstructed from incoming X-ray photons. MOS CCDs, on the other hand, or Metal Oxide Semiconductor CCD arrays, only receive 44% of the beam as they are partially blocked by other instruments aboard the *XMM-Newton*. They each consist of 7 chips, stacked so that they slightly overlap to prevent gaps in the data. However, this placement leads to fluorescence which must be filtered out of the source information, to be explained later. At the time of the observation, though, one of the chips in the MOS1 CCDs was out of use; consequences of the outage were small, and could be compensated for by other means.

Collecting data with three detectors has many advantages, not limited to the ability to exploit the properties of the two kinds of detector chips. For example, MOS cameras are much more sensitive to low energies than PN cameras--regions where oxygen, neon, and iron lines are expected to dominate the spectrum. PN, rather, has a larger range of sensitivity, extending from about .2 to 15 keV, has an unobstructed view, and does not suffer from fluorescence resulting from stacked chips. Combining the three sets of data obtained during a single observation provides beneficial diversification in the data where the shortcomings of one detector may counterbalance the other.

Once the data are collected by EPIC and stored in the *XMM-Newton* archive, one may begin systematically processing each data set using the European Space Agency's (ESA's) specialized software package developed specifically for *XMM-Newton* observations called Science Analysis Software, or SAS. The software was created by the Science Operations Centre (SOC) in conjunction with the Survey Science Centre (SSC) in an effort to supply users with a complete set of X-ray data processing tools. Still, the software is to be used with the HEASoft package developed by NASA's HEASARC, or High Energy Astrophysics Science Archive Research Center, for programs like Xspec and additional analysis utilities like FTOOLS. Together, SAS and HEASoft allow processing, reduction, and analysis of X-ray data. This bundle is the sole software used throughout this research, with the exception of the imaging software, Ds9, and a platelet smoothing script.

## DATA PROCESSING

This section describes the technical aspects of data processing using SAS and FTOOLS, and may serve as an intermediate guide to the user wishing to perform spectral analysis. More detailed explanations may be found in the *XMM-Newton* Users Guide, while a brief outline of the details below is available in the *XMM-Newton* ABC guide; both are available on the Web.

To begin, after SAS is installed and one has retrieved the data files from the *XMM-Newton* archive, specific variables must be input in order to operate the program smoothly. Each process in Linux runs within its environment, or a set of characteristics with which a program may interact. SAS requires the user to manually set the environment with the commands either entered individually at the prompt or written into a file and sourced before each use of SAS (commands may be found in the *XMM-Newton* ABC Guide). Once the environment variables are sourced, one may run SAS.

The retrieved data come in two groups downloaded from the archive as file directories: the Observation Data File (ODF) and the Pipeline Processing files (PPS). The latter of the two has been “pipeline processed” by the SSC and hence arrives with the current calibrated event files, X-ray source lists, etc. As an aside, an event file contains specific information from an observation in the form of a Flexible Image Transport System, or FITS, file; it is input into SAS for manipulation and later analysis. If the PPS is up-to-date, one may begin analysis using the information contained therein. Otherwise, one must manually process the raw EPIC event files listed in the ODF directory, including not only the observation data, but also “housekeeping” files describing the condition of the telescope at the time of data collection like the radiation monitor and spacecraft files. Processing the ODF is a multi-stepped task, initiated by unpacking the ODF directory using the *gunzip* or *gzip* commands. Next, the current calibration files, or CCFs, must be

downloaded from the *XMM-Newton* Web site using the SAS task *cifbuild*. As the telescope ages, wear of the on board electronics must be accounted for in the calibration files. For example, early observations from the X-ray observatory were conducted at peak detector sensitivities. Years after its launch, however, sensitivity has decreased due to normal, space-based processes. Therefore calibrating new ODFs with old calibration files would lead to errors in the analysis. Likewise, the SSC actively works to improve its technologies, thus the latest CCFs contains these upgrades which typically go hand in hand with the SAS version released at that time. *cifbuild* automatically downloads the complete list of CCFs stored in what is known as the Calibration Access Layer, or CAL. If the CAL has changed for any reason, one must re-pipeline the data to ensure the most accurate data survey. After the CCF list is complete, to continue pipelining the ODFs one must append housekeeping files and calibration files to the raw event files using the SAS tasks *odfingest* and *emchain/emproc* (for MOS event files) and/or *epchain/epproc* (for PN event files). At this point, the bundled files are ready for prepping and analysis with SAS.

*XMM-Newton's* Science Analysis Software was designed to be an integrated package of FITS utilities with the ability to manipulate astronomical data in a number of useful ways. After initializing SAS, one may call a chosen task by either selecting it from the pop-up GUI or via the command line. With this in mind, the next step in preparing data for spectral analysis is to invoke the task *xmmselect*, which loads the event file with user-selected options and presents the user with several choices, like creating a light curve, creating a spectrum, etc. Although background will be thoroughly discussed shortly, it is useful to briefly discuss a form of background filtering at this time. Soft protons unrelated to the object of study will sometimes enter the telescope and appear as real data. Fortunately, these contaminants ordinarily appear as flares and may easily be removed by examining the appropriately binned light curve and subtracting times of excess photon events; this process is called temporal filtering.

In addition to filtering for time, one may also filter for specific energies, regions, and even good pixels. The *xmmselect* task allows one to enter a “selection expression,” or a criterion for choosing only specific data. Entries must use traditional logic operators, as explained in the *XMM-Newton* Users Guide, and may be applied to the photon energy, also called pulse height (PI), the pattern describing how the photons hit the detector, say by illuminating a single pixel, two pixels, etc. called the PATTERN, and to specific filtering criteria, like rejecting pixels deemed bad during the observation and pixels within CCD chip gaps. Experts from SSC and SOC recommend filtering MOS and PN data in imaging mode for PATTERNS less than or equal to pattern 12 and pulse heights from .2 - 12 keV and .2 - 15 keV for MOS and PN, respectively (Snowden et al. 2009). For spectral analysis, the most conservative form of event filtration, FLAG==0, should be included in the selection expression. This keyword removes pixels deemed unfit for analysis in three scenarios: eliminated on board the satellite; identified in the CCF; and identified on a per mission basis. Each of these is stored in an event file labelled with a “BADPIX” extension. Another type of filtering, spatial filtering, is dependent upon which areas are desired for analysis. Users may create a selection expression consisting of the region characteristics defined in either sky coordinates or detector coordinates by way of the command line or by extracting the region in the imaging program Ds9. Using sky coordinates as opposed to detector coordinates which vary between the two MOS and PN, allow the user to easily select the same region in each instrument with little hassle. Additionally, when analyzing an extended source, one must exclude any point sources from the region by removing corresponding circular regions greater than or equal to the point spread function, or PSF, thus accounting for any smearing caused by the point sources. For the “background-subtraction” method of spectral analysis, a sky background and source region must be selected separately for background analysis.

The final steps in creating a spectrum are fairly straightforward, including generating a PI file of the events chosen from the user-inputted selection expression and making the corresponding response files. SAS will automatically produce the spectrum after the appropriate spectral bin sizes and spectral channel minima and maxima are provided. Occasionally the SAS task responsible for calculating the PI files' scaling factors, *backscal*, must be run independently of the PI creation. The BACKSCAL keyword stored inside the PI file determines how two spectra when loaded together should be normalized relative to one another. Differencing the source region's geometric area and the combined value of the CCD gaps and bad pixels gives the correct scaling factor generated by *backscal*. Xspec, the X-ray spectral fitting package supplied by HEASARC, cannot use the PI file alone. Instead it must be loaded into the program with a response file. There are two files required to completely account for the spectral response of the EPIC telescopes: the photon Redistribution Matrix File (RMF) and the Ancillary Response File (ARF). Both are discussed below.

Because of the intricacies involved in utilizing electronics to detect incoming photons, the energies stored in event files are not necessarily the raw energies of the photons. A CCD detector sends event information through specific channels determined by the location of the photon interception. Ideally, a uniform source should register a constant number of photons in each channel, but in reality different channels have different probabilities of detecting photons. The varying sensitivities must be compensated for in some way. In Xspec, this difference is accounted for by including a response file--made up of the RMF and ARF--along with the PI file. The ARF file calculates effective area including vignetting, EPIC filter transmission, and CCD quantum efficiency as a function of energy (de la Calle 2009). The full response file is created by multiplying the spatially independent RMF with the ARF. A mathematical model, or function, appears very different when loaded with an instrumental response file, see Fig. 9. However, the inclusion of both the PI and response files are necessary for accurate results.

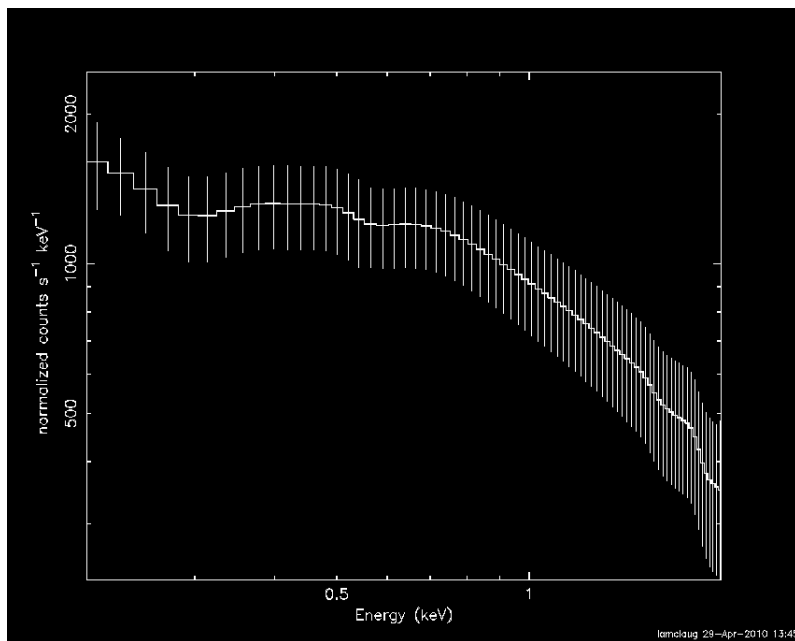


**Figure 9.** Power law fit with PN spectral response file. The familiar appearance of a power law is transformed when fit with a response file. Here, a power law with photon index equal to 1.4 has been “folded” with the PN response.

The final step in SAS processing is to group the files together in a format compatible with Xspec. Grouping may be accomplished using the FTOOLS command *grppha*. In the least, the grouped file must consist of the RMF coupled with the PI file, however, many files may be tied together in this way. For background subtraction, for instance, the grouped FITS file must contain the PI file, ARF, RMF and background PI file. In addition, the PI data may be binned when using *grppha*. The output file is now ready for spectral analysis and modeling.

## MODELING

The goal of spectral analysis is to find a model which provides an adequate fit to data collected in an observation. A model is a mathematical representation of the physical processes (see X-ray Emission in SNRs) taking place in the observation to produce the shape of the data. For SNRs, there exists a limited number of models describing radiation received by X-ray detectors. A few of those applicable to the research of SNR G296.8-0.3 are presented below.

*Raymond-Smith Model:* Perhaps the least complex model included in this section, the Raymond-Smith Model is used for hot, diffuse plasma. Ionization equilibrium is assumed, which doesn't necessarily mean all particles are ionized, but that ionization and recombination rates have equalized. There are four main parameters: plasma temperature ( $kT$ ); metal abundances; redshift ( $z$ ); and normalization. The elemental abundances mentioned here are given as a ratio to cosmic, or solar, abundances measured in the sun and meteorites found in the Solar System (Arnaud et al. 2010). C, N, O, Ne, Mg, Si, S, Ar, Ca, Fe, and Ni are included in this measurement because they are relatively common, mostly made in the alpha processes of stars.

*Non-Equilibrium Ionization (NEI) Model:* This model assumes a constant temperature and includes one additional parameter than the Raymond-Smith model--the ionization timescale ( $\tau$ ). Because most SNRs are not in ionization equilibrium, one must account for the fact that the ionization state of the plasma advances with time. The ionization timescale may be derived by

multiplying the time since the remnant was shocked by the post-shock electron number density,  $n_e$ ; thus  $\tau$  has units of  $\text{s cm}^{-3}$ .

*Plane-parallel Shock Model (Pshock)*: Like the NEI model, Pshock assumes a constant temperature. It is used to model plane-parallel shocked plasma, and therefore can describe plasma with a range of ionization timescale values, from  $\tau_l$  to  $\tau_u$ , the most recently shocked to the originally shocked value, respectively. For example, the shock front will have  $\tau_l = 0 \text{ s cm}^{-3}$ .

*Photoelectric Absorption Model (phabs)*: To account for the amount of interstellar gas absorbing photons in the line of sight of the source, one may multiply the photoelectric absorption model by the models listed above. The only parameter in this multiplicative model is the hydrogen column density ( $N_H$ ) given in units of  $10^{22} \text{ atoms cm}^{-2}$ .

## EPIC BACKGROUND

To have good, confident results, one must be able to increase the signal-to-noise ratio of a data set to a value which ensures the source information is accurate and credible. For *XMM-Newton* observations, nearly all contamination arises from X-ray photons other than the source contacting the detectors. Before action can be taken to extract these bad components, one must first understand how EPIC receives these events. For example, some background photons are focused by the mirrors of the telescope, and so they should only be detected in the field of view (FOV), as opposed to the outer perimeter of the detector chips. Knowing why the noise exists--and how it affects the detector--facilitates its removal from analysis.

There are three constituents which make up what is collectively called the EPIC background: electronic noise; particle background; and photon background. The first component, electronic noise, may be easily overlooked because it only produces event counts in energies less than .2 to .3 keV, a regime which is rarely used in spectral analysis. This type of background may appear as bright pixels in images, and for the PN can come from CAMEX readout noise--a device used to amplify incoming signals. The amount of readout noise may vary as much as 10% between observations, but due to the range of affected energies, even this amount of variation may be dealt with by simply ignoring energies less than .5 keV.

Particle background contributing to the EPIC background noise may be attributed to two different sources: soft protons and cosmic ray induced particles. Soft protons, according to Carter and Read, are produced by "magnetospheric reconnection events trapped by the Earth's magnetosphere." *XMM-Newton* has a highly elliptical orbit and as the observatory approaches perigee, the frequency of soft proton flares increases. In fact, soft proton flares affect up to 40% of observation time. Because they are low keV events originating outside of the telescope, the soft protons must be focused through the telescope's mirrors, but

they are typically constant across the detector. Consequently, to analyze the spectrum of soft proton events, one must fit flare data without the instrumental response files. Carter and Read (2007) report that the soft proton spectrum can be fit above .5 keV with a broken power law, placing the break energy at 3.2 keV. Since their detection is limited to the field of view, soft proton flares may easily be mistaken for valid photons. Fortunately, most soft protons reach the detectors in a flaring event, meaning many particles are intercepted by the telescope in an isolated interval of time, from hundreds of seconds to hours (De Luca and Molendi 2002). Therefore a quick look at the event's light curve will reveal at which times the detector received abnormal photon counts. A simple temporal filter will extract time intervals affected by soft protons, however some may remain between flaring events.

Cosmic rays, or high energy particles traveling at relativistic speeds, are too energetic for *XMM-Newton* telescope's mirrors to focus, nevertheless, they play a large role in the EPIC particle background. Because cosmic rays can penetrate the telescope casing, they are able to reach the detector and create a charge in the CCDs, causing instrumental fluorescence called the quiescent particle background. This happens wherever a cosmic ray intercepts the detector, and so depending on the CCD make-up, fluorescence of one element may appear in one site but not another: see Fig. 10. MOS CCDs, for example, are made of silicon and so they fluoresce Si-K; PN is not and thus unaffected by Si fluorescence. MOS instrumental fluorescence occurs at 1.5 keV and 1.7 keV, for Al-K and Si-K, respectively, with some high energy contributions from Cr, Mn, Fe-K, and Au. Likewise, PN's spectrum shows line fluorescence at 1.5 keV for Al-K and additionally Cu, Ni, Zn and K at higher energies. Since the quiescent particle background happens internally, it is unaffected by vignetting. The MOS CCDs, which are partially obstructed, still record any events outside the field of view, or outFOV, therefore *any* detection in this region must be attributed to cosmic ray induced events. Also, an aluminum filter wheel covers the detectors and rotates between filters.

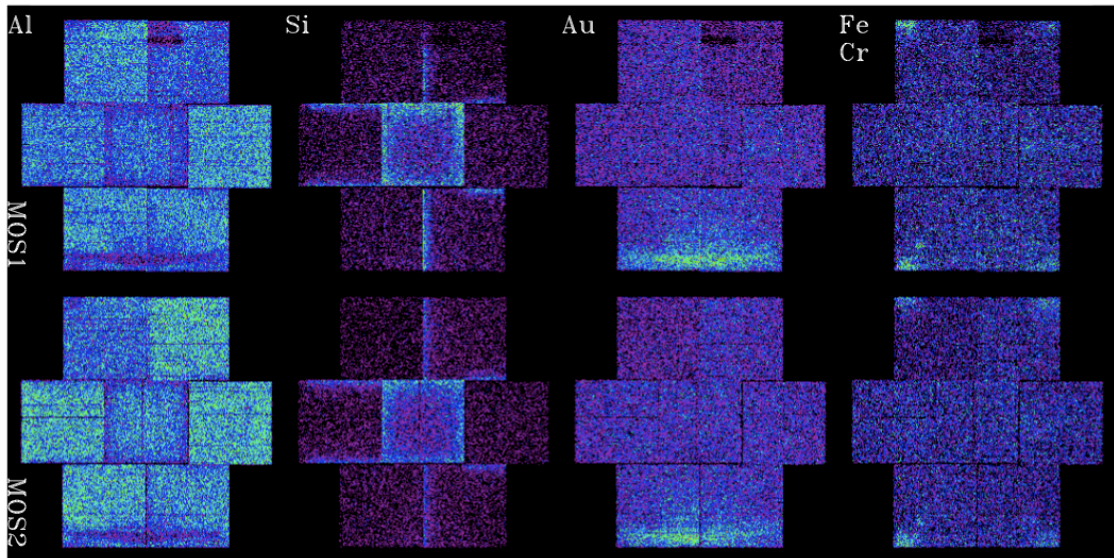


**Figure 10.** Spatial variation in the quiescent particle backgrounds in MOS. Filter wheel closed observations showing the major fluorescent lines. *Top:* MOS1. *Bottom:* MOS2. *From left to right:* Al, Si, Au and FE + Cr. *Image courtesy of Kuntz and Snowden 2008.*

The filter wheel may be set so that it is in the closed position, thus preventing any X-rays from reaching the CCDs. Data taken during this time exclusively show particle fluorescence (see Fig. 11), and so may be used to model and account for the quiescent particle background from source spectra.

In a routine observation, the *XMM-Newton*'s FOV is not limited to the object of study, unless it is a truly large and diffuse X-ray region. For most cases, there exist other X-ray bright features visible in the collected data, both bright and faint. Regardless of their luminosities, these sources have a large enough presence to pollute observations. This last category of EPIC background events are true photons and so they are focused by the mirrors. The photon background contribution in observations is significant and can be assigned to separate sources depending on energy. The soft X-ray component, for example, originates in the Galactic disc, Galactic halo, and the Local Bubble, a region of sparse interstellar medium believed to have been created by supernovae millions of years ago. In addition, a process called solar wind charge exchange, where ions traveling in the solar wind become neutralized when contacting the Earth's exosphere, add to the low energy background sources (Carter and Read 2007). Unwanted hard X-rays, on the other hand, come from the cosmic X-ray background (CXB), with 80%-90% attributed to active galactic nuclei, or AGN. At 3 keV, the CXB may be modeled with a power law of photon index  $1.41 \pm .06$  and a normalization of  $2.46 \pm .09$  photons  $\text{cm}^{-2} \text{s}^{-1} \text{sr}^{-1} \text{keV}^{-1}$  (De Luca and Molendi 2004). All X-ray photon background is vignettted, or subject to the same spatial variations of the telescopes as source photons, and contributions are either in the FOV of the scopes or out of the FOV and reflected off the mirrors into the detectors (Carter and Read 2007). Fluctuations in the EPIC photon background happen on large scales because of their Galactic and extragalactic origins, so they are not spatially dependent on the detectors, with the exception of AGN appearing in the FOV as point sources.

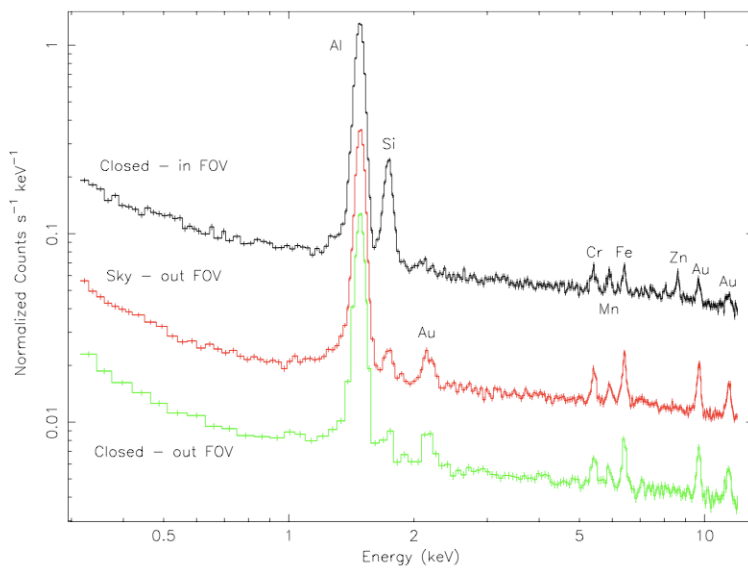


**Figure 11.** Quiescent particle background from MOS1. Data presented is from the FOV region with the filter wheel in the closed position (black), from the *out FOV* region with the filter wheel opened but pointed at blank sky (red), and from the outFOV region with the filter wheel closed (green). The filter wheel closed *out FOV* spectrum has been rescaled three times for visual purposes (De Luca and Molendi 2004). *Image courtesy of De Luca and Molendi 2004.*

All of the components discussed above are present in data taken aboard the *XMM-Newton* observatory and contribute to the noise seen in spectra. Nevalainen et al. (2005) did a thorough investigation into EPIC background; their plots of the background contributions as functions of energy are shown in Fig. 12. Background sources may mask real data and reduce spectral resolution. Nevertheless, there are a few ways to enhance the signal in such instances.

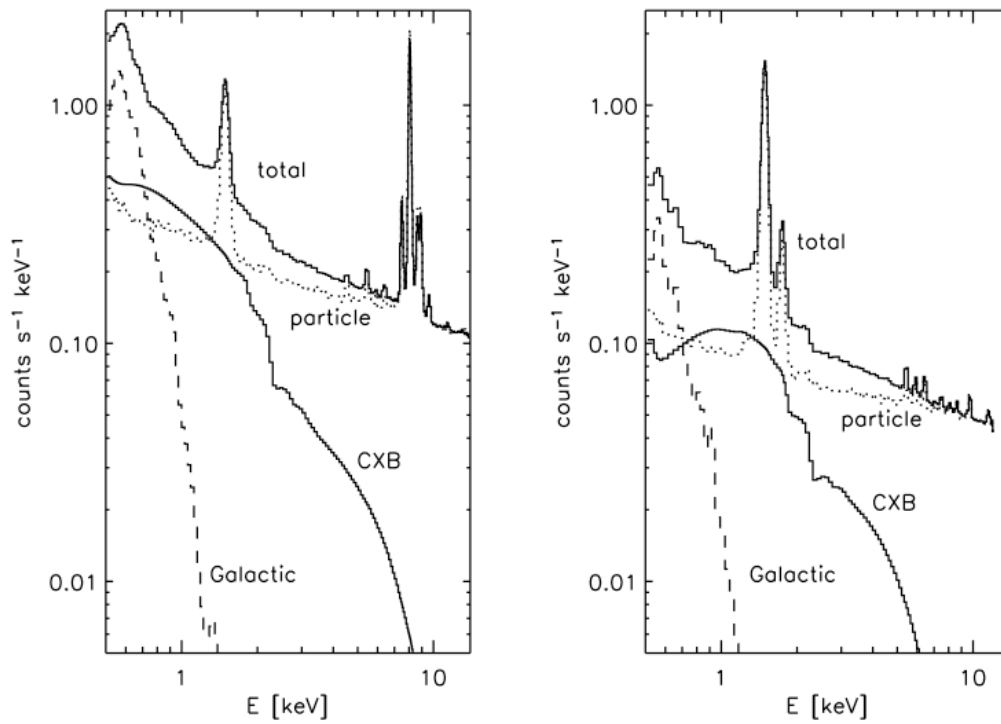


**Figure 12.** Background contributions in PN and MOS. Nevalainen et al. modeled the total backgrounds for PN (*left*) and MOS (*right*) by merging both filter wheel closed observations and observations filtered for point sources and diffuse emission (2005). *Image courtesy of Nevalainen et al. 2005.*

### SNR G296.8-0.3

Now that sufficient background in supernova remnants has been provided, the focus of this thesis will shift to the object of this current research, the X-ray morphology and spectrum of SNR G296.8-0.3. The name, G296.8-0.3, is derived from the remnant's position in Galactic coordinates. In this coordinate system, the Milky Way's center is at a longitude  $l = 0^\circ$ , and the plane of the Galaxy at latitude  $b = 0^\circ$ . Therefore, G296.8-0.3's Galactic coordinates are  $l = 296.8^\circ$  and just below the central plane of the Galaxy at  $b = -.3^\circ$ , placing it in the southern hemisphere's constellation Crux. This translates to a RA  $11^{\text{h}} 58^{\text{m}} 25^{\text{s}}$  and dec  $-62^\circ 36'$ . Although little may be seen in optical wavelengths (see Fig. 13), particularly  $\text{H}\alpha$  (Walker, 2006), G296.8-0.3's morphology has previously been observed and studied in both radio and infrared energies, with radio showing the most detail. This remnant is highly atypical, displaying a double-ringed structure and a large diameter for its relatively young age as suggested by Gaensler et al. (1998). Theories concerning G296.8-0.3's peculiar evolution include expansion into anisotropic media, or expansion into what is known as a "super bubble," or the complete disruption of an asymmetric progenitor. Thus by studying G296.8-0.3, one is hopeful to gain insight into any of these three phenomena.

The biannular structure of G296.8-0.3 (G296) proves to be a very curious feature, demanding the attention of several researchers. Identification as a SNR is credited to Large and Vaughan (1972), who based its classification on its shell-like structure and spectral index in radio energies. Whiteoak and Green further confirmed remnant status at .843 GHz using the Molonglo Observatory Synthesis Telescope (MOST) as an addition to the MOST supernova remnant catalogue. Studies entered new territory when Hwang and Markert (1994) reported the very first X-ray observations of G296 as part of an investigation of five known radio remnants in the Carina spiral arm using the *ROSAT* Position Sensitive Proportional Counter (*PSPC*). The  $4\sigma$

detection of this object led to the estimation of a column density,  $N_H$ , equal to many times  $10^{21} \text{ cm}^{-2}$ , similar to the value given by HI measurements via the 21 cm line (see below). According to Hwang and Markert, this remnant should lie much further than 4 kpc away when compared to the relatively low  $N_H$  calculation of a remnant in the same part of the sky with an assumed similar count rate. In addition, Hwang and Markert identified an appreciable X-ray flux originating in the western part of the remnant corresponding to the region of peak radio flux, but could not conduct spectral analysis due to poor signal to noise.

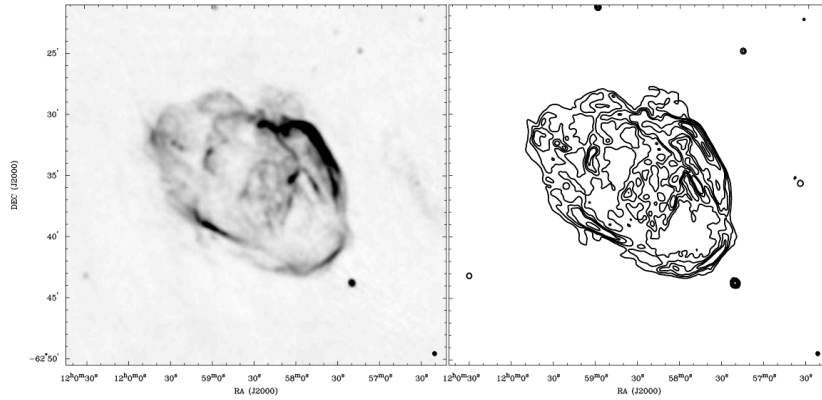
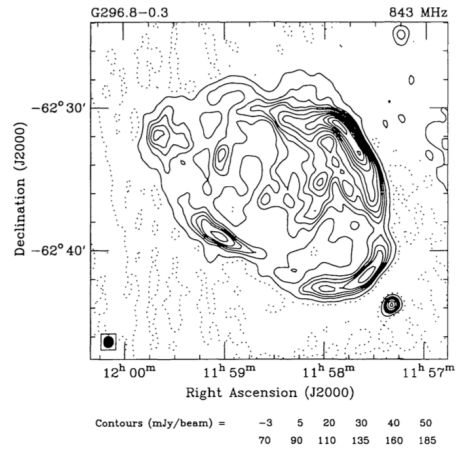
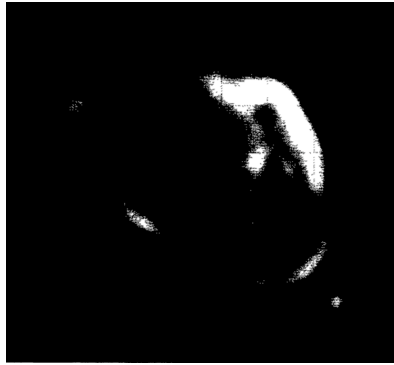
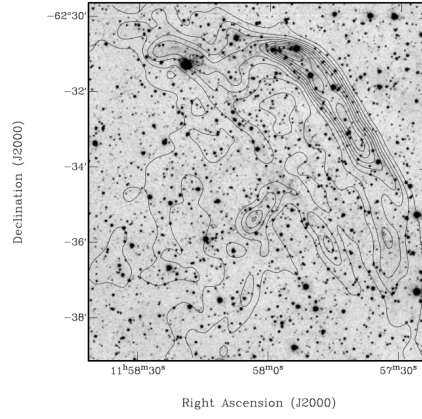
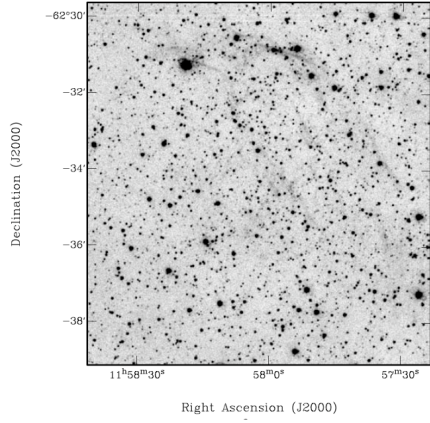
The most thorough radio investigation of G296 to date was performed by Gaensler, Manchester and Green (1998) including distance estimations, polarization measurements, and column density calculations. This team used data obtained from the Australia Telescope Compact Array, or ATCA, at 1.3 GHz to derive properties of the remnant from synchrotron radiation occurring in ultrarelativistic electrons at the shock front. Morphology of G296 was given in detail, describing a multiple-ringed structure with a “slightly curved strip of emission, beginning beyond the remnant’s northern boundary and extending up, or close, to its southern perimeter.” In addition, they confirm the northwestern location of peak radio flux, while noting the eastern portion is much more faint. Gaensler et al. also extensively studied the HI velocities of absorbing clouds in the line of sight to the remnant. They then fit these values to a Galactic rotation model given by Fich, Blitz, and Stark (1989) to derive a kinematic distance of  $9.6 \pm 0.6$  kpc. Using this distance, they calculated a swept up mass of  $\sim 500n_I M_\odot$ , where  $n_I$  is the ambient density in  $\text{cm}^{-3}$  (Gaensler et al. 1998) averaging 0.1 to 1 particle per  $\text{cm}^{-3}$  (Culhane and Sanford 1981), ultimately inferring the remnant is in the Sedov phase of evolution. Finally, using Sedov formulations and  $n_I = 0.2$  (Frail et al. 1994), they arrived at an age of  $(10 \pm 2) \times 10^3$  years. Each of the parameters derived from the papers above has been summed in Table 1. Explanations of symbol notation may be found in the table’s footnote (or in the symbol index at the beginning of this work). Additionally, images from these works may be found in Fig. 13.

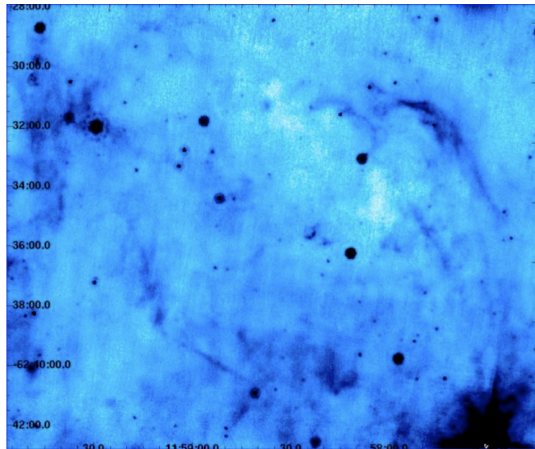
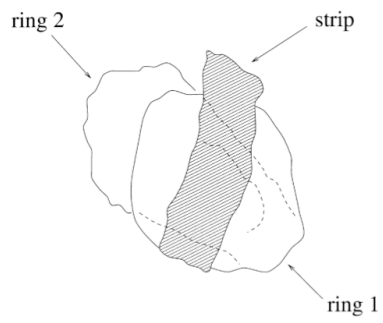
**Table 1.** A summary of G296.8-0.3. Parameters taken from the references listed in the table’s footnotes are found below. Note “ $\Sigma$ - $D$ ” signifies a distance derived from the surface brightness-diameter relation, a formula deemed to have substantial uncertainties (Green 1984).

<b>Freq./Energy of Obs.</b>	<b><i>Flux</i> (<math>S_0</math>)</b>	<b><math>\Theta</math> (‘ × ‘)</b>	<b><i>Distance</i> (kpc)</b>	<b><math>\nu^\alpha</math></b>
.843 GHz <sup>(1)</sup>	9.2 Jy	20 × 14	N/a	N/a
.408 - 5 GHz <sup>(2)</sup>	9 Jy (at 1 GHz)	14’ (assuming spherical dim.)	9.7 ( $\Sigma$ - $D$ )	-0.6
1.3 GHz <sup>(3)</sup>	7 ± 0.3 Jy	18’ × 12’	9.6 ± 0.6	-0.65 ± 0.08
0.1 - 2 keV <sup>(4)</sup>	N/a	14’(assuming spherical dim.)*	~10	N/a

$S_0$  - integrated flux density;  $\Theta$  - angular diameter;  $\nu^\alpha$  - spectral index, N/a - parameter not reported  
References: (1) Whiteoak & Green 1996; (2) Caswell et al. 1975; (3) Gaensler et al. 1998; (4) Hwang & Markert 1994  
\*Taken from (2)

**Figure 13.** G296.8-0.3 pictured in other works. G296.8-0.3 pictured in other works. *First row: left:* optical images taken by the Anglo-Australian Observatory/UK Schmidt Telescope H $\alpha$  survey showing the very faint northwest strip of emission; *right:* same image but with radio contours overlain. *Images from Walker 2006.* *Second row:* MOST images from Whiteoak and Green 1996, left: G296; *right:* MOST contours with level values listed below photo. *Third row:* from Gaensler et al. 1998, *left:* detailed radio image from ATCA; *right:* contours from ATCA data. *Fourth row: left:* also from Gaensler et al. 1998, cartoon description of the remnant; *right:* *Spitzer* image of G296.8-0.3 at 24  $\mu$ m, from Borkowski, 2007.





Gaensler et al. (1998) proposed three explanations for the biannular morphology of G296.8-0.3: G296 is two different objects; the progenitor had biannular symmetry; or it is a consequence of anisotropic interstellar media. The first suggestion was deemed unrealistic because of sheer probability--according to HI measurements throughout the remnant, all regions must be at about the same distance, therefore the chances of two systems reaching end points around the same time in the same area is highly unlikely. The second proposition ascribes the double-shelled shape to either the ejecta's expansion into the main sequence wind of a rotating progenitor, since Bjorkman and Cassinelli (1993) and Owacki, Cranmer and Blondin (1994) theorize such a phenomenon would focus the wind along the equatorial plane, or that the SNR simply (and inexplicably) resumed its biannular propagation into isotropic CSM. Lastly, Gaensler et al. supported the anisotropic media proposition by describing two wind-blown bubbles connected by a tube of lower density; in this case, all three regions are in the plane of the sky, thus observers see two shells and a strip of emission stacked upon one another. Currently, this is where the mystery remains--no known papers have since been written attempting to elucidate the curious morphology of G296.8-0.3. For this reason, Borkowski proposed (2007) to view the remnant in more detail using the European Space Agency's X-ray observatory, *XMM-Newton*.

By citing motivations like the strange morphology, hopes for spectral analysis, and yet another observation--this time in infrared--revealing peak flux coincident with previous radio observations, Borkowski initiated the research presented in this thesis. The new observation referenced in his paper was performed with the *Spitzer* Space Telescope at 24  $\mu\text{m}$  and with *Spitzer's* IRAC at 8  $\mu\text{m}$  (Fig. 13); the former displayed very strong emission in the same locations as the ATCA data, while the latter proved to be very weak--a trend explained by thermal dust emission. Studies of Galactic and Magellanic Cloud remnants support the notion that dust heating is caused by immersion in hot plasmas, so one should see X-ray bright

regions corresponding with radio and infrared. Furthermore, Borkowski suggested the presence of thin, bright filaments in these two energies could not be produced from a nonradiative shock propagating through a uniform medium, but that a radiative shock travels too slowly to produce the hard X-rays seen with ASCA. However, detailed spectral analysis of G296.8-0.3, including the investigation of shock velocities, ionization ages and plasma temperatures in X-ray, should greatly illuminate this remnant's history.

### ANALYSIS OF G296.8-0.3

Upon approval of the proposal, in February 2006 the *XMM-Newton* collected over 20 ks of data while trained on G298.6. However, this data was very noisy (see Fig. 14), and so was only used as a “practice run” for spectral analysis until the arrival of the second set of data, which proved much more useful. Although suffering from heavy flaring from 45 ks to 60 ks, the data from the second observation contained much less contamination. After temporal filtering of the soft proton flares (see “Data Processing”), around 44 ks of good time intervals (GTI) remained. To maximize signal to noise, the cutoff for acceptable GTIs was very conservative--roughly 25 counts s<sup>-1</sup> for PN and 8 counts s<sup>-1</sup> for MOS, leaving 58% and 85% of the original data remaining in PN and MOS, respectively. All attempts at analysis were filtered according to *XMM-Newton* guidelines, including FLAG==0 and PATTERN less than or equal to 12. In addition, while generating the ARF, the option for “extended source,” as opposed to point source, was selected to increase accuracy of the FOV’s effective area. Regions for analysis were selected in only the brightest X-ray locations, limited to the northwestern limb of G296’s shell: see Fig. 15. Background regions were mostly chosen to be elliptical annuli about the source region, and to an extent did include some very faint source X-ray emission, also displayed in Fig. 15. However, source intensities in the background region were expected to be so low that their contributions to background spectra were negligible.

Since it is customary, and in most cases sufficient, to do a simple background subtraction technique to create source spectra, we began by selecting the same source and background regions in PN, shown in Fig. 16, and MOS. We then prepped the data for analysis by grouping the source and background PI files with the corresponding ARF and RMF. In Xspec, spectra from all three instruments were loaded together, each with their individual response files and background-subtracted source data. Before preparing the spectrum, we

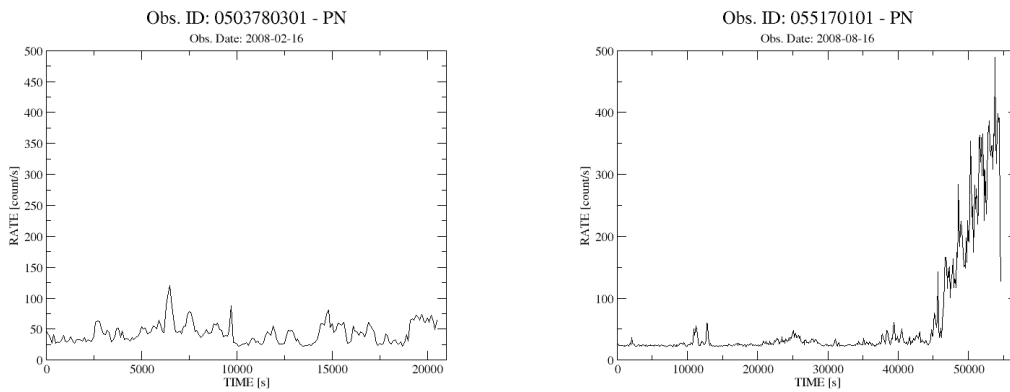


**Figure 14.** Light curves of two G296.8-0.3 observations. *XMM-Newton* conducted two observations on SNR G296.8-0.3, one gathering 21 ks of data in February 2008 (*left*) and one of 60 ks of data in August 2008 (*right*). The first observation suffered from heavy background noise. Only the second observation was used for spectral analysis. Each light curve has 100 cts/s in each bin.

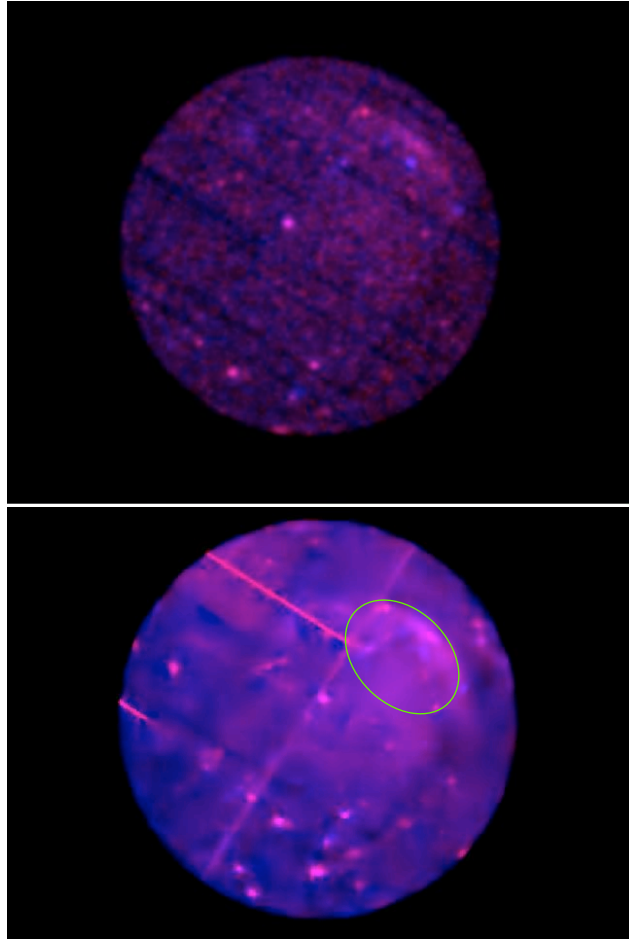


**Figure 15.** G296.8-0.3 in *XMM-Newton* observations. PN, MOS1 and MOS2 images merged together; included energies are .5 - 1.095 keV (red) and 1.95 - 2.00 keV (blue), these ranges are chosen so there are an equal number of counts in each color representation. In MOS, 1.457 - 1.517 keV and 1.710 - 1.780 keV have been completely excluded to omit Al-K and Si-K fluorescence from the images, while Al-K energies have been omitted from PN. *Top:* Image smoothed with Xspec's gaussian smoothing feature. *Bottom:* Here the image has been smoothed using a "platelet smoothing" technique developed by Dr. Rebecca Willett, a researcher at Duke University. These images show the areas of greatest X-ray intensities--mostly in the northwestern limb of the shell. The green oval represents the region chosen for X-ray analysis.

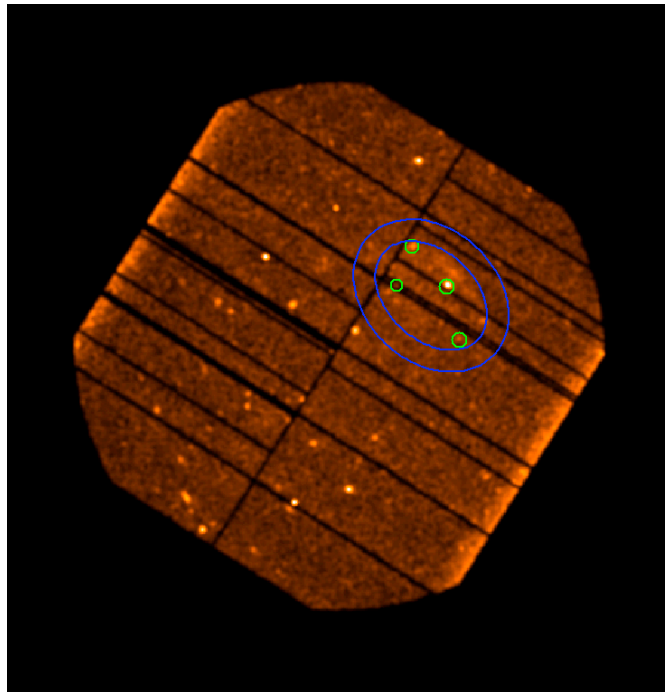


**Figure 16.** Background and source regions. Using the PN as an example, for most of the analysis, the source region consisted of the inner ellipse outlined here in blue, while the background was taken to be the outer elliptical annulus. Green circles indicate omitted point sources. Dark lines in this image are bad pixels, like chip gaps, filtered out by the FLAG==0 keyword. Shell emission, although faint, is visible just below the top of the inner ellipse.

displayed G296 in several energy ranges and found the SNR evident in energies from about .5 keV to 2 keV, therefore we ignored the other energies in our analysis. At this point we were ready to simply model the data. However, after background subtraction only an average of 16% of the data was determined to be source counts. While this is lower than was expected, we continued with modeling, but switched to “gehrels weighting,” a system of weighting appropriate for low count rates, since many channels now contained few or no counts.

Because G296.8-0.3 is very large, the simplest explanation for its considerable area is that it has been expanding into the interstellar medium for a long time. An old remnant, one in either the late Sedov phase or radiative phase, would be either in ionization equilibrium or at least approaching it, so we started our fits with a photo-absorbed Raymond-Smith model. Since no fits were achieved with believable parameter values, say  $kT \leq 4.0$  keV for one, fitting progressed to the NEI model. At that point, the ionization timescale,  $\tau$ , could be used to decide the ionization state of the remnant;  $\tau$  must be at least a few  $10^{12}$  cm<sup>-3</sup> s for a remnant to be in ionization equilibrium (Reynolds 2008). Fits with phabs\*NEI (photo-absorbed NEI model) were considered poor and gave large errors (Fig. 17), but the models consistently gave low values for  $\tau$ , around  $10^{10}$  cm<sup>-3</sup> s, implying the existence of a surprisingly young shock front. However, when the Pshock model was applied, most fits continued to give large errors, inconsistent ionization timescales, and unrealistically high temperatures ( $kT > 3$  keV). After fitting with three different models and obtaining no real physical results, we deemed the background subtraction to be at fault and began an investigation into the background of the EPIC instruments.

From the previous fittings, we noticed the Si-K instrumental fluorescence line, despite using background-subtraction, remained very strong in the data. In addition, there was a “hole” in the data around 1.5 keV which we later attributed to an over-subtraction of the Al-K line. These phenomena may be

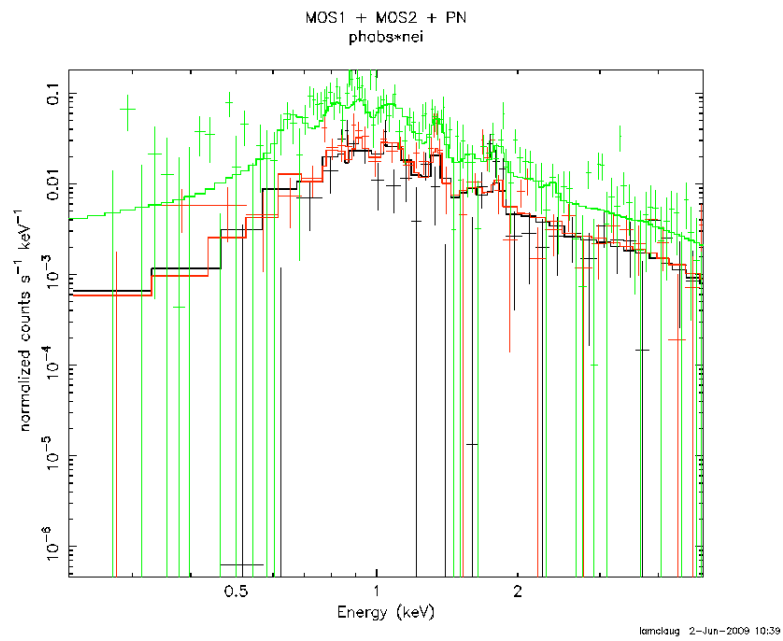


**Figure 17.** Photo-absorbed NEI model on background-subtracted data. The fit above is typical for the background-subtracted data from PN (green), MOS1 (red) and MOS2 (black). Errors are large and parameters are very unlikely ( $\tau \sim 10^{10} \text{ cm}^{-3} \text{ s}$ ). The long lines on the data points (crosses) signify upper limits to those values.

understood by examining Fig. 10. Si-K is strong in the borders of the center CCD chip, where the analysis region is located. Furthermore, the placement of the elliptical annulus used for the background region is relatively devoid of such fluorescence, resulting in under-subtraction of the Si-K line from the spectrum. For the Al-K line, the case is exactly the opposite. Aluminum fluorescence appears when the CCD casing, made of aluminum, is struck by a cosmic ray particle. Therefore, the closer to the edges of the CCDs, i.e. in the vicinity of the background region, the more occurrences of Al fluorescence. Clearly, the spatial variations of the quiescent particle background were too complex for simple background-subtraction and another means of increasing the signal to noise ratio was needed. This brought us to the use of what are known as “blank sky” backgrounds.

After some investigation, we discovered event files available on the *XMM-Newton* calibration and background Web page which offered a solution to the quiescent particle background. These files, called blank sky backgrounds, are a superposition of images taken throughout the *XMM-Newton* mission which are either devoid of sources or have had any obvious emission removed. A file exists for each instrument and their corresponding modes, filters, etc. Also, all have been pipelined with the latest CCF after their production. In addition, the files come filtered for times of high background, having an upper count rate threshold of 60 cts s<sup>-1</sup> for the PN and 2 cts s<sup>-1</sup> for MOS. To compensate for any “holes” created during point source removal, both unfilled (point source areas are left absent of data) and refilled event lists are available. The latter file consists of point source holes which have been filled by replacing the empty pixels with values randomly chosen from pixels close to the extracted region. Finally, one may choose event files taken from either the Galactic center, or away from this region, referred to as anti-Galactic center (Carter and Read 2008).

For our analysis, we needed medium filtered, full frame blank sky event files. These were chosen to be refilled and anti-Galactic center since our object is at  $l \sim 297^\circ$ . In preparing the data, we incorporated the same criteria used for creating the source PI file, including the `FLAG==0` selection expression and a `PATTERN` corresponding to only single- and double pixel-events. Despite the conservative default temporal filtering of the PN blank sky files, we found it necessary to filter even further, and reduced the average counts per second to 25--the same as the source data. Once filtering was complete, we extracted the exact source region used in the background-subtraction analysis from the blank sky files by converting the region dimensions, which were originally calculated in sky coordinates, to detector coordinates using the SAS task *esky2det*. Next, the blank sky PI files were created. However, because the blank sky event files are a compilation of several individual pointings at different times during the mission, keywords such as the observation date could not be included within the file. This prevents SAS from creating a `BACKSCAL` value during the PI generation since bad pixels may depend on the time the exposure was taken (see Data Processing). To circumvent this problem, we simply manually assigned the `BACKSCAL` value computed for the original X-ray source region to the blank sky files. Upon grouping, we combined the same source PI file, ARF, and RMF, but this time the background file was exchanged for the new blank sky spectrum.

Although we were still using the background-subtraction technique, we had compensated for the spatial variation of the Si and Al fluorescence by using the same detector region for both the source and the blank sky background spectrum. With high expectations, we began modeling the new data. Upon first glance of the blank sky background-subtracted data we noticed a majority of the data points were being extremely over-subtracted. This effect was originating from the large difference in count rates of the source data, which was only one exposure compared to the many combined exposures making up the blank sky event files. To compute the factor to which the new background must be normalized, we calculated the ratio

of blank sky count rate to source count rate in the particle-dominated region of the spectra. As demonstrated in Fig. 12, hard X-ray contributions, specifically above 9 and 10 keV, are solely from particle background, and since the rate at which the detector registers this source is fairly constant throughout times of data collection, one may use the count rates in this range to renormalize the blank sky spectrum to the source spectrum. Once this factor had been found individually for each instrument's spectrum, we used the Xspec functions, *corfile* and *cornorm*, to apply them to their appropriate spectra.

Results from our meticulous blank sky method initially looked very promising; by using the new renormalized background files the percentage of counts from the source was boosted up to an average of 72%, a vast improvement from the 16% obtained by using the elliptical annulus background region in the same exposure as the source region. This time, the Pshock model appeared to give the best fits with the smallest error; one of the better fits is pictured in Fig. 18. Although decent fits could be made from forcing the plasma temperatures to values lower than 1 keV, the majority of attempts gave  $kT = 1.0\text{-}2.0$  keV and  $\tau \sim 10^{11}$  cm<sup>-3</sup> s. After several modeling efforts, though, we noticed a couple of worrisome trends. The hard X-ray portion of the spectrum, from about 1.5 to 2.0 keV was unable to be fit no matter which model we used or how we constrained the parameters. Even more important, acceptable fits were generated only when the PN normalization was allowed to differ from MOS values, sometimes up to 30%. It has been noted in *XMM-Newton* documentation that PN and MOS sensitivities do vary, but this is compensated for in the calibration files. A difference greater than 10% must be attributed to some error large enough to strongly compromise the integrity of the data. However, at the time of analysis, we were unaware of what factors could cause this discrepancy, therefore, we discontinued this line of processing.

Recently, a more thorough inspection of the Xspec task *cornorm* revealed a small miscalculation in our work which may have been the error of the blank sky analysis. The *cornorm*, or correction

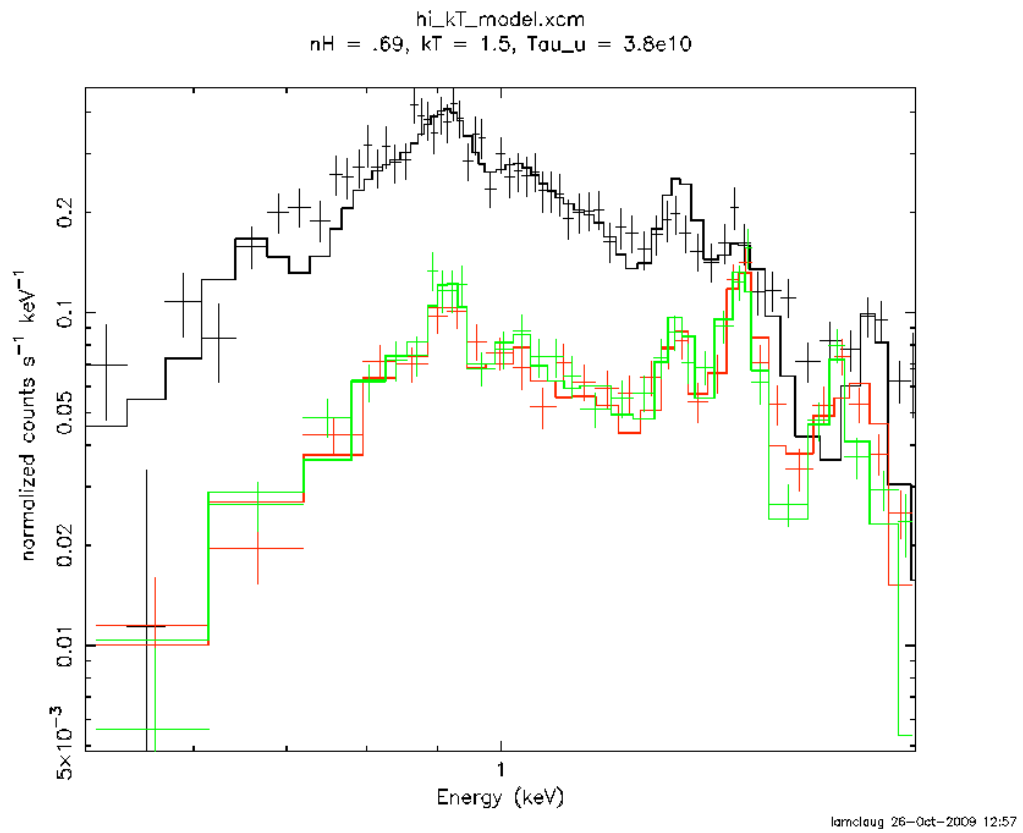


**Figure 18.** Photo-absorbed Pshock model fitted to blank sky background subtracted data. The fit above represents one of the better fits to the blank sky background-subtracted spectrum. The data was modeled using phabs\*pshock,

normalization, factor should have been calculated by differencing the particle count rate of the original blank sky file with the source particle count rate, then dividing the result by the count rate of the desired *corfile*, or correction file. In our case, the *corfile* was the blank sky background PI file, so the *cornorm* should simply be 1 minus the ratio of the blank sky to source particle count rates. However, when we first computed the *cornorm*, we miscalculated by a sign difference. The result was not obvious at the time, but its implications may have been enough to prevent accurate fitting of the data. Due to time constraints, we have not returned to this technique to apply the correct *cornorm*.

## FINAL ANALYSIS

With the past two attempts proving unsuccessful, we began analyzing the background to investigate the reason the normalizations between the MOS and PN dramatically differ. Our conclusion naturally focused on the difference in the behavior of MOS and PN with respect to cosmic ray induced events and how this may affect individual continuum flux. Recognizing our previous inability to thoroughly subtract the background noise from the source signal due to low count rates, we shifted to a method in which we included both background and source. By utilizing a set of files downloaded from the *XMM-Newton* Website called “filter wheel closed,” or “closed-cover” background files, we were able to model the quiescent particle contribution for each instrument individually. While particularly important for the Si K and Al K line strengths, using the filter wheel closed (FWC) files also allowed adjustment of the particle flux and hence provided a potential solution for any PN underfitting.

As explained in the EPIC background section, the FWC files are a collection of merged images taken with the aluminum filter wheel in the closed position thus preventing any X-ray photons from contacting the detectors. Only cosmic ray particles are energetic enough to penetrate and so only the quiescent particle background, including fluorescent line emission, appears in the FWC spectra. The data were collected for each EPIC instrument at times throughout most of the *XMM-Newton* lifetime, usually at the end of object observations. As a result of their scattered observation times, creating a single RMF to describe the specific condition of the detectors during each observation is an extremely complex undertaking and has not yet been performed at the time of this thesis. To compensate for the missing response files, while using the FWC data we applied the same RMF and backscale as those calculated from the source data. Recall the backscale factor is computed as the geometric area of the observation region minus any chip gaps

and bad pixels; these values are unknown for each of the FWC observations, and so the backscale value may introduce slight, perhaps negligible, errors in the EPIC data. However, the effects of simply copying the backscale for MOS1 may be more significant, for at the time of the G296 observation this detector contained an entire bad chip, some of which included roughly a sixth of the source region. The backscale value for the MOS1 FWC spectrum then is about a sixth less than it should be. While the results of the MOS1 backscale error have not been thoroughly investigated, they are believed to be insignificant to first-order in the spectral fits.

In addition to the particle background, to more precisely estimate the background spectrum we researched the true sky background X-ray emitters in the vicinity of G296.8-0.3, including cosmic X-ray background (CXB) and Galactic ridge X-ray emission (GRXE). The GRXE is defined as diffuse X-ray emission attributed to unresolved sources in the Galactic plane. Because G296 lies at a latitude of  $b = -0.3$ , the GRXE may have a large background contribution. Using research performed by De Luca and Molendi (2005), we modeled the CXB with a photon index of  $1.41 \pm .06$  and computed the normalization to be  $2.85 \times 10^{-5}$  photons  $\text{cm}^{-2} \text{s}^{-1}$ . Furthermore, we applied an absorption to the CXB valued at  $N_{\text{H}} = 1.6 \times 10^{22}$  atoms  $\text{cm}^{-2}$ , which we cited from the *Chandra* X-ray Center's proposal planning toolkit called "Colden" (Smithsonian Institution, 2004). This program displays the column density toward the most distant Galactic hydrogen cloud, hence bounding the dimensions of the Milky Way. Because the CXB originates from objects outside the Galaxy, it must be absorbed by all the neutral hydrogen produced by various Galactic sources along the line of sight in a given direction. Combining this with the works of Revnivtsev and Sazanov (2007) and Revnivtsev, Molkov, and Sazanov (2006), we approximately represented the Galactic ridge as an absorbed power law of photon index  $\Gamma = 2$ , and normalization  $3.34 \times 10^{-5}$  photons  $\text{cm}^{-2} \text{s}^{-1}$  with a reasonable assumption of  $N_{\text{H}} = .8 \times 10^{22}$  atoms  $\text{cm}^{-2}$ .

As seen in Fig. 12, beyond 2 keV EPIC spectral X-ray background contributions come from only two sources: CXB and the quiescent particle background. Note that Fig. 12 was created using data collected from a high Galactic latitude, therefore no GRXE would be evident in this figure. G296.8-0.3, on the other hand, may include additional background from the GRXE. Therefore, there are three components to the X-ray sky background spectra at  $\geq 2$  keV: particle; CXB; and GRXE. By modeling these three at high energies, we may figure the amount by which the individual instrumental particle normalizations differ between the FWC and source observations. After all, after the GRXE and CXB models have been applied to G296's sky background spectrum, only the quiescent particle photons are left to be fit. Using the same particle spectrum's shape derived from FWC data, we found the correct particle flux by simply allowing the normalizations to float while fitting at energies from 2 - 5 keV. That is, above any soft X-ray contributions but below parts of the spectrum where high-energy fluorescence takes place.

For completeness, we finished modeling G296's sky background spectrum by fitting a thermal component to low energies. The values produced from this fit are unimportant, since we only wanted the shape of the background spectrum, not to model its origin. The complete sky background is shown in Fig. 19.

Once the sky background was modeled with the adjusted FWC particle normalizations, we applied this model to G296's source spectrum. Before we could accurately model the source, though, we had to replace the adjusted sky background particle fits with source particle fits adjusted with the same normalization constant to make up for the difference in particle fluorescence and instrumental effective area. Any counts remaining above the sky background model must be attributed to the source then, and may be modeled: see Fig. 20. However, one may see from this figure there are regions where the source is dominated by the background, mostly at low energies. Again, beginning with a simple ionized plasma model, we

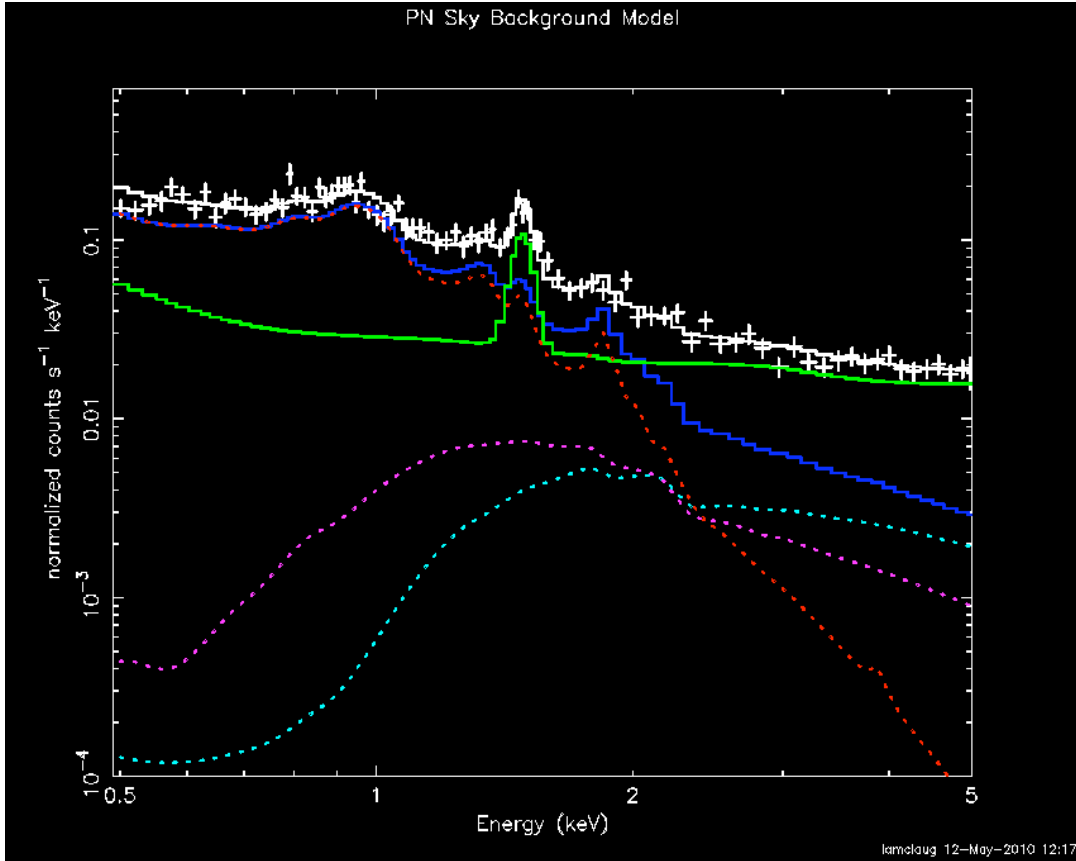


**Figure 19.** PN sky background. Although modeled in *Xspec* for all EPIC instruments, to clearly show each background component only the PN spectrum and fits are shown. *White crosses:* PN sky background data; *white solid line:* complete background fit; *blue solid line:* low energy thermal model + CXB + GRXE; *green solid line:* quiescent particle model; *red dotted line:* soft X-ray thermal model; *magenta dotted line:* GRXE;

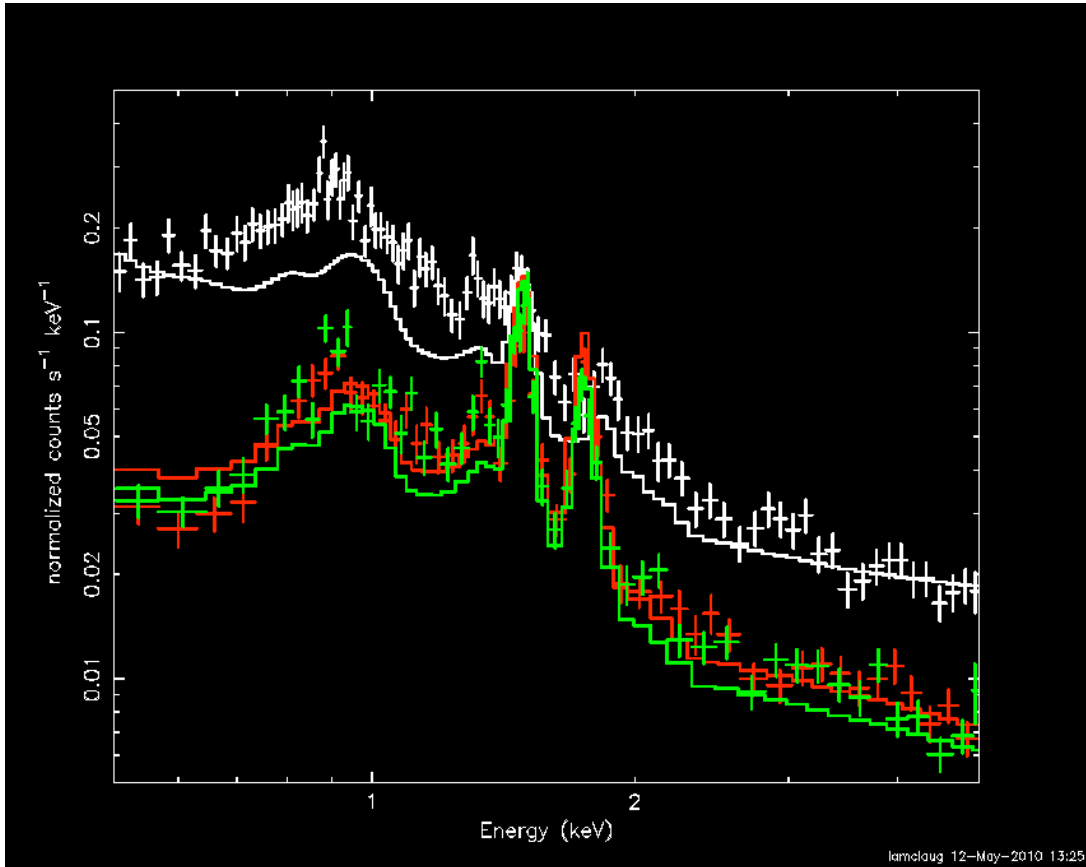


**Figure 20.** PN and MOS fit with sky background model. Log-log plot of the PN (*white*), MOS1 (*red*), and MOS2 (*green*) fitted with the sky background model with the adjusted FWC particle fits (*solid lines*). Notice the sky background domination in MOS at low energies and the difference between PN and MOS in this region. Data has been binned for visual purposes.

progressively fit more complex models until a good fit was reached. Because we were now including both unbinned source and sky background data, we switched from  $X^2$  to C-statistics (see Cash 1979). Despite our efforts, underfitting of the PN continued, although not to such a degree as before; this is demonstrated with an absorbed Pshock model in Fig. 21. The ill-fitting normalizations made it impossible to model all three instruments simultaneously *and* find a good fit. Because the PN had the most counts (at least twice as many as the MOS), we applied an absorbed Pshock model to the sky background-modeled PN data only. Time allowed for only a few fits, but most of the best fits gave similar values; the values for one fit are:  $kT = 1.54$  (1.04, 2.45) keV,  $N_H = 0.835$  (0.749, 0.912)  $\times 10^{22}$  cm<sup>-2</sup>,  $\tau = 1.38$  (1.02, 2.10)  $\times 10^{10}$  cm<sup>-3</sup> s, and norm = 3.02 (1.83, 5.27)  $\times 10^{-4}$  (see Fig. 22). Errors are given at the 90% confidence interval for C-statistics. Modeling MOS1 and MOS2 simultaneously gave similar results.

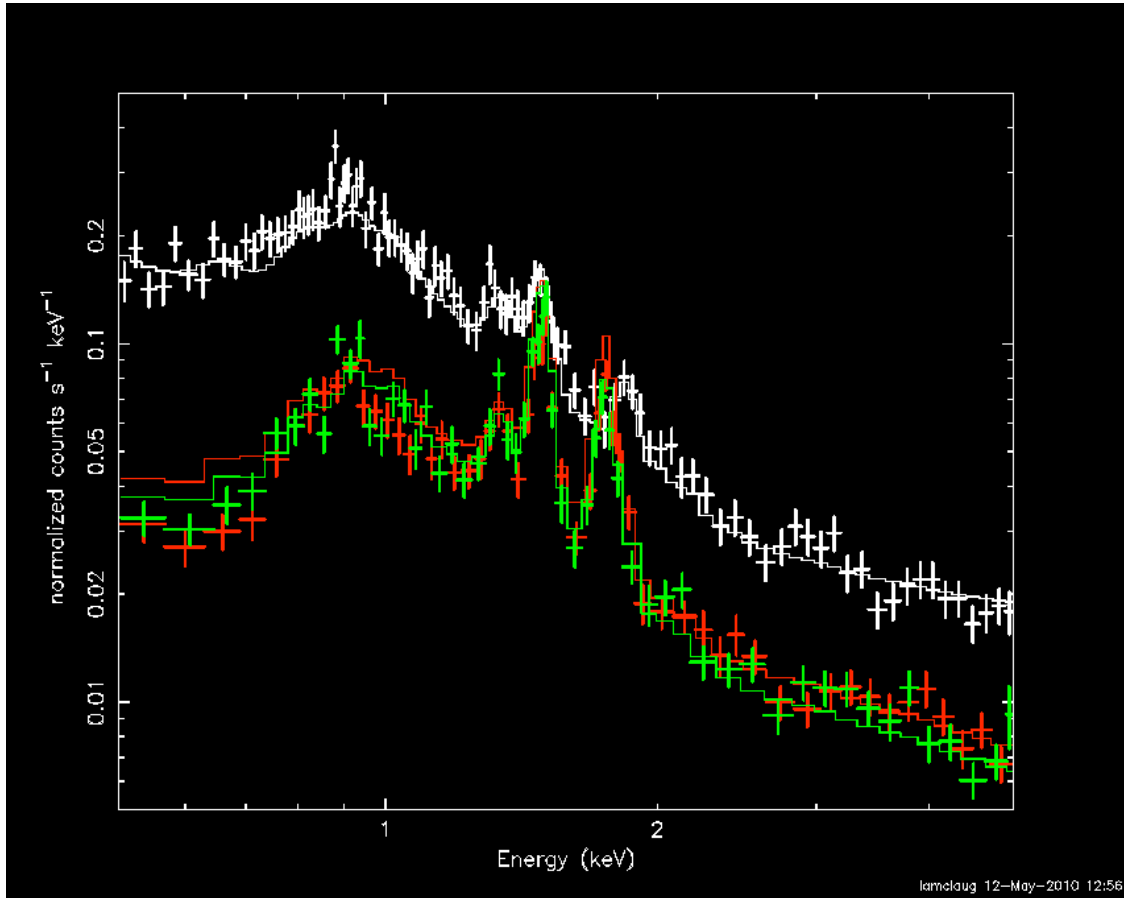


**Figure 21.** PN underfitting. Log-log plot of source data (*crosses*) and photo-absorbed Pshock + background fits (*solid lines*) for PN (*white*), MOS1 (*red*) and MOS2 (*green*). Data has been rebinned for display purposes. The purpose of the fit is to demonstrate the underfitting of PN at low energies, and consequently the over fitting of MOS.

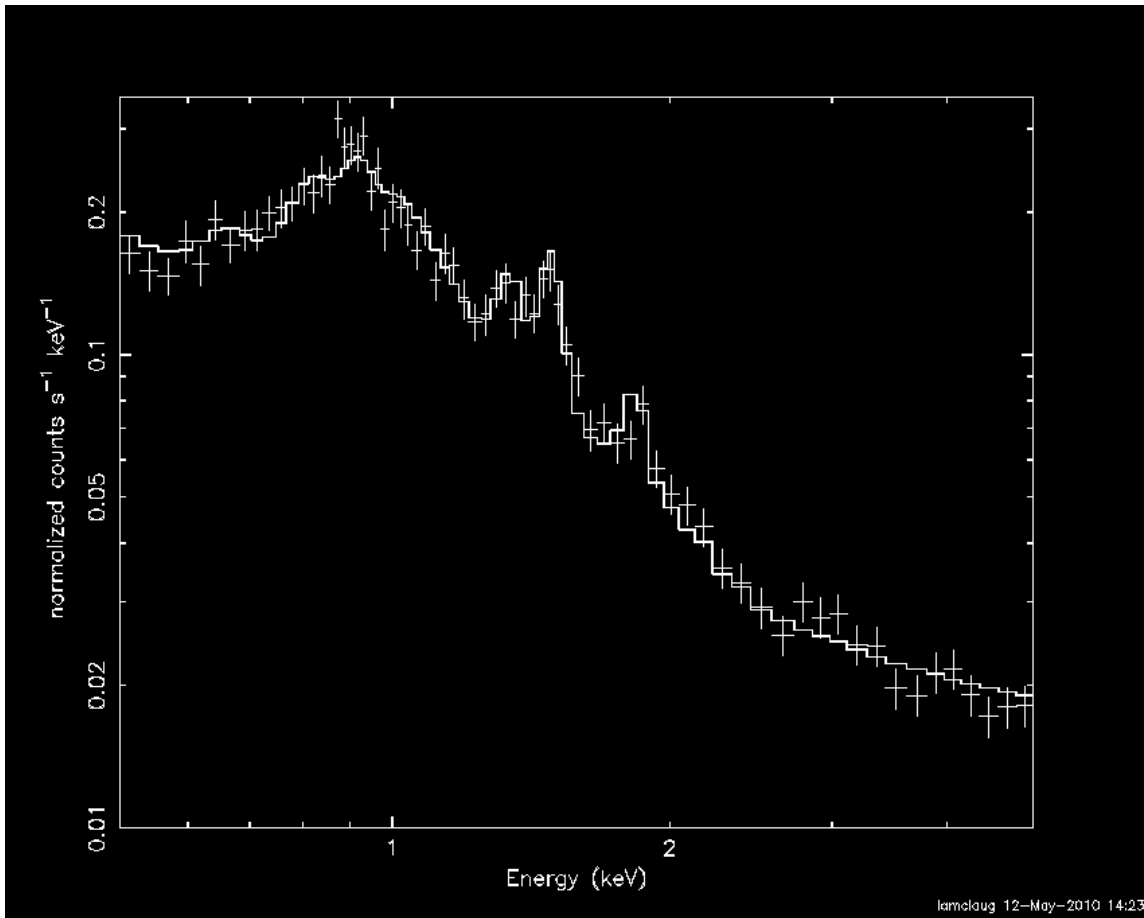


**Figure 22.** PN data fit with absorbed Pshock model. This Pshock model was applied only to the PN data and gave the following parameter values:  $kT = 1.54 (1.04, 2.45)$  keV,  $N_H = 0.835 (0.749, 0.912) \times 10^{22}$  cm<sup>-2</sup>,  $\tau = 1.38 \times 10^{10} (1.02 \times 10^{10}, 2.10 \times 10^{10})$  cm<sup>-3</sup> s, and  $\text{norm} = 3.02 (1.83, 5.27) \times 10^{-4} \times 10^{-4}$ . Errors are given at the 90% confidence interval for C-statistics. Data has been rebinned for visual purposes.

## RESULTS

Using Reynolds (2008), we derived the values explained below from the model-derived parameters. For all calculations, we have adopted the 9.6 kiloparsec distance,  $d$ , and estimated an angular radius of 9 arc minutes ( $R = 7.9 \times 10^{19}$  cm) for G296.8-0.3 as provided by Gaensler et al. (1998). Also, we have left all the calculations in terms of the 9.6 kpc distance so that the distance  $d = d_{9.6} \times 9.6$  kpc. Noting the absorbed Pshock fit for PN gave abundances equal to solar and assuming the unshocked ISM is neutral and the post-shocked materials are fully ionized, in other words, the upstream mean mass per proton mass is  $\mu_1 = 1.4$  while the downstream is  $\mu_0 = 0.6$ , we computed the shock velocity to be  $1.14 (.940, 1.44) \times 10^8$  cm s<sup>-1</sup> using the equation

$$u_8 = .922(kT/1\text{keV})^{1/2},$$

where  $u_8$  is given in  $10^8$  cm s<sup>-1</sup>. Furthermore, in computing the shock velocity we have assumed the electron and ion temperatures have equilibrated. Still, we note that for a shock velocity of  $u \gtrsim 10^8$  cm s<sup>-1</sup> the ion temperature is estimated to be greater than the electron temperature, thus underestimating the shock velocity. From here, we accounted for two scenarios: G296 is still in the free expansion phase (absent of shock deceleration) and G296 is in the Sedov phase and may be described with Sedov dynamics.

*Free Expansion:* To find an upper limit on the age of the remnant, we used a simple formula describing the age of the remnant in the free expansion phase, i.e. assuming a constant shock velocity,  $u$ , up to the observed radius,  $R$ . Thus the real age,  $t$ , may be calculated using  $t < R/u$ . Therefore,  $t < 6.9 (5.5, 8.4) \times 10^{11}$  s, or  $\sim 22,000$  yrs. Note that if the shock velocity was larger

in the past, i.e. the front has slowed to its present value, the age of the remnant is less than 22,000 years.

Upon obtaining the real age of the remnant, a mean post-shock electron density,  $n_e$ , could then be calculated for G296 still assuming it is in the Free Expansion phase. Rearranging the ionization age equation,  $\tau = n_e t$ , we find  $n_e = \tau/t = .020$  (.012, .038)  $\text{cm}^{-3} d_{9.6}^{-1}$ . Because  $t$  is an upper limit,  $n_e$ , and therefore  $\tau/t$ , must be a lower limit. An alternate way to find the post-shock density may be calculated using the X-ray emission measure ( $EM$ ) found from the spectral fit using emission contributions from both electrons and ions. According to the fitting software, *Xspec*, the normalization parameter, denoted “norm,” is

$$norm = 10^{-14} (EM) (4\pi d^2)^{-1}$$

or

$$EM = 10^{14} 4\pi d^2 norm$$

where the emission measure is defined as

$$EM \equiv \int n_e n_i dV.$$

$n_i$  is the mean post-shock proton or hydrogen density. If the remnant is dominated by ISM instead of the ejecta, which is implied by the fit, one may assume cosmic composition in which an estimated 10% of atoms have 2, rather than 1, electrons. In consideration of this new abundance,  $n_e$  must be 20% greater than  $n_i$ , or  $n_e = 1.2n_i$ , therefore

$$\begin{aligned} EM &= (1.2)^{-1} \int n_e^2 dV \\ &= (1.2)^{-1} n_e^2 V. \end{aligned}$$

Equating this expression for  $EM$  with the aforementioned one and solving for  $n_e$  gives the rms density:

$$n_{\text{rms}} = (10^{14} 4\pi d^2/V)^{1/2} (\text{norm})^{1/2}.$$

In order to arrive at a numerical estimation, we assumed the volume to be an ellipsoidal region with a depth  $h$  calculated to be the value of a chord's length situated at  $.5R$  from the center of the sphere and running parallel to the diameter (see Fig. 23). Using this volume estimation,  $V = 3.1 \times 10^{59} \text{ cm}^3 d_{9.6}^3$  and gives an rms density of  $n_{\text{rms}} = 0.036 (.028, .048) \text{ cm}^{-3} d_{9.6}^{-1}$ . This value is within the error bars of  $n_e$ . Also, by assuming a strong shock, or one in which substantial energy is not lost due to the acceleration of significant amounts of particles to relativistic velocities, the shock compression ratio,  $r$ , may be taken to be 4. Because the PN fit gave cosmic compositions, we computed the upstream hydrogen density,  $n_1$ , using  $n_1 = n_e/(1.2r) = .0042 (.0025, .0079) \text{ cm}^{-3} d_{9.6}^{-1}$ . Finally, by assuming the current SNR volume,  $V$ , to have once been homogeneous ISM with a constant density  $n_1$ , we estimated the swept up mass using

$$M_{\text{SNR}} = 1.4m_p V n_1,$$

where  $V = 4\pi R^3/3$  and is the estimated volume of the entire remnant. We found  $M_{\text{SNR}} = 10.0 (6.2, 20.0) M_{\odot} d_{9.6}^2$ . Of course, the dimensions of G296.8-0.3 are not spherical, so there are large errors on this calculation.

*Sedov:* Because it is likely for such a large remnant to have accumulated more ISM than its initial mass, more realistic parameters can be obtained accounting for shock deceleration. In this case, we used the following Sedov equations to calculate the age of the remnant,  $t_{\text{Sedov}}$ , and its explosion energy,  $E$ , as if it were in the Sedov phase using the following equations:

$$u = .4R/t_{\text{Sedov}};$$

$$R = 1.15(E/n_1)^{1/5} t_{\text{Sedov}}^{2/5}.$$

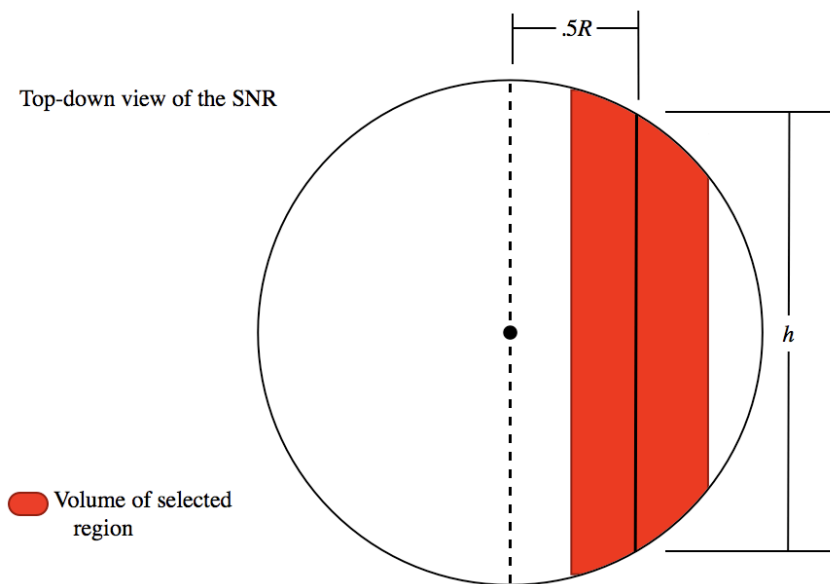


**Figure 23.** Volume of selected region. Simplified top-down view of G296.8-0.3 for purposes of calculating volumes. In order to estimate post-shock rms density and remnant mass, we used a spherical volume. The region in red represents the volume of the SNR selected for spectral analysis, which was calculated as an elliptical cylinder with depth  $h$ .

Thus the age of the remnant is  $t_{Sedov} = 2.8 (2.2, 3.4) \times 10^{11} \text{s } d_{9.6}$ , or about 8900 years. Applying this to the post-shock electron density, we found  $n_{e,Sedov} = .049 (.030, .095) \text{ cm}^{-3} d_{9.6}^{-1}$  and hence  $n_1 = .010 (.0063, .020) \text{ cm}^{-3}, d_{9.6}^{-1}$ . The explosion energy was then calculated to be  $E_{Sedov} = 4.6 (2.0, 15.0) \times 10^{50} \text{ ergs } d_{9.6}^2$ . Finally, we computed  $M_{SNR} = 25 (16, 49) M_{\odot} d_{9.6}^2$ .

## CONCLUSIONS

Upon inspection of G296's X-ray data, there is no evidence for a pulsar. The brightest X-ray regions are to the Northwest, and are most likely where the fast moving shock wave has met with regions of much higher densities. Because there are no other X-ray bright regions associated with the radio shell, we believe the eastern and southern edges of the remnant have yet to encounter these densities, and thus are expanding at larger shock velocities than is the Northwestern region.

Using the values calculated from the PN fit after the sky background and quiescent particle background had been modeled, we could infer several properties of G296.8-0.3. Before we did so however, we recognized the values derived from the model had large uncertainties due to low signal to noise. Still, our analysis was as precise as possible given the data we used. For more accurate results, a longer observation is required to boost the amount of counts. Nevertheless, examining the results obtained by the fit revealed a decelerated shock velocity; considering the large radius of G296 and that the calculated shock speed was 1,100 km/s, compared with the accepted post-supernova particle velocity of 5,000 to 10,000 km/s, the remnant's front has to be slowing. Thus, calculations performed using Free Expansion phase concepts only provide limits: a lower limit for the true age with respect to the ionization age and an upper limit on  $\tau$ .

The more plausible explanation for G296's large radius and shock velocity is that it is currently in the Sedov phase of evolution in which it has expanded into a uniform medium and swept up its own mass of interstellar material. Not only would this account for the slowing shock velocity, but also the high mass calculations as the remnant would have had ample time to accumulate material. Whether core collapse or Type Ia, the amount of material found in the remnant is most likely greater than the progenitor's mass, unless created by a super massive star which is not supported by our fits as we have found cosmic abundances. If

the progenitor was supermassive, it is likely the derived abundances would have been more specific to the progenitor's stellar makeup instead of cosmic. In addition, while still low, the Sedov values for the upstream density are more probable than those calculated for Free Expansion. Finally, the explosion energy derived from Sedov formulae are within errors of the standard emitted kinetic energy for SNe, or  $10^{51}$  ergs.

As explained in the introduction of G296.8-0.3, thin radio and infrared filaments observed in the remnant are not consistent with a Sedov-like environment, that is, a uniform density throughout its evolution. So even more likely is the theory proposed by Gaensler et al.: the remnant is rapidly expanding into a low density bubble blown-out by the progenitor's wind or even another SN (1998). Supplementing their theory, we predict a scenario in which only recently has the shock front reached the higher density interstellar material created by the aforementioned progenitor. This would have allowed G296.8-0.3 to expand with little loss in particle velocities up to the point of reaching the edge of the bubble. At that stage, ionization of the material would have increased dramatically coupled with a decline in continuum temperature. Therefore the ionization timescale from our model would mostly be applicable from the period in which the shock front reached the dense cloud making up the bubble's perimeter to the present time, necessitating an adjustment in the value of the radius used for most of the computations mentioned above. Conducting such an alteration would boost both the post-shock and pre-shock densities to those closely resembling ISM or CSM densities, in addition to increasing the real age and likely decreasing the SNR mass. Overall, this theory provides a better explanation for parameters derived in our plane-parallel shock model fits.

In the future, more work is necessary to confirm the curious properties of G296.8, not limited to longer observations to decrease signal to noise. Solutions for the double-ringed structure and consistent high temperatures shown in our fits and those of other researchers have only begun to be explored. While our derivations seem to support the existence of a low density bubble blown out by either the progenitor or other

SNe, sufficient evidence has yet to be presented which confirms these hypotheses. However, with the data we now possess, it may prove useful to conduct a two-temperature fit to the current region: a high temperature model for the low density region, and a low temperature model for the more dense, highly ionized area. A good fit may help support this theory. We finally note that the values presented here are only preliminary and will be more thoroughly investigated after the conclusion of this thesis.

## REFERENCES

- Arnaud K, Dorman B, Gordon C. 2010. *Xspec: An X-ray Fitting Package*.
- Axelrod TA. 1980. *Type Ia Supernovae*. Austin: University of Texas.
- Barbon R, Ciatti F, and Rosino L. 1973. *Astron. Astrophys.* 29:57.
- Bjorkman JE, Cassinelli JP. 1993. *Ap.J.* 409:429.
- Borkowski KJ, Lyerly WJ, Reynolds, SP. 2001. *Ap.J.* 548:820.
- Branch D. 1990. *Supernovae*. New York: Springer-Verlag, Inc.
- Brewton-Parker College. *Math and Natural Sciences*. (2010 April version). URL: [http://www.bpc.edu/mathscience/chemistry/images/periodic\\_table\\_of\\_elements.jpg](http://www.bpc.edu/mathscience/chemistry/images/periodic_table_of_elements.jpg).
- Carter JA, Read AM. 2007. *Astron. Astrophys.* 464:1155.
- Cash. 1979. *Ap.J.* 228:939.
- Caswell JL, Clark DH, Crawford DF. 1975. *Australian J. Phys., Astrophys. Suppl.*, 37:39.
- Chevalier RA. 1990. *Supernovae*. New York: Springer-Verlag, Inc.
- Culhane JL, Sanford PW. 1981. *X-ray Astronomy*. Charles Scribner's Sons.
- De La Calle I. (ed.). 2009. *XMM-Newton: User Guide to the XMM-Newton Science Analysis System*.
- De Luca A, Molendi S. 2002. *Mem. S.A.It.* 73:1.
- De Luca A, Molendi S. 2004. *Astron. Astrophys.* 419:837.
- Dyer K. 2001. *Thermal and Non-Thermal Emission in Supernova Remnants*. North Carolina State University.
- Fich M, Blitz L, Stark A. 1989. *Ap.J.* 345:931.
- Frail DA, Goss WM, Whiteoak JBZ. 1994, *Ap.J.* 437:781.
- Gaensler BM, Manchester RN, Green, AJ. 1998. *Mon. Not. R. Astron. Soc.* 296:813.
- Green DA. 1984. *MNRAS*. 209:449.

- Harkness RP, Wheeler JC. 1990. *Supernovae*. New York: Springer-Verlag, Inc.
- Hwang U, Markert, TH. 1994. *Ap.J.* 432:819.
- Jones T, Rudnick L, Jun B. 1998. *PSAP*. 110:125.
- Kuntz KD, Snowden, SL. 2008. *Astron. Astrophys.* 478:575.
- Large MI, Vaughan AE. 1972. *Nature Phys. Sci.* 236:117.
- Lochner J. 2010. *Pulsars*. (April 2010 version). URL: [http://imagine.gsfc.nasa.gov/docs/science/know\\_12/pulsars.html](http://imagine.gsfc.nasa.gov/docs/science/know_12/pulsars.html).
- Manchester RN. 1994. *Astron. Soc. of Aus. Proc.* 11:1.
- Marschall L. 1988. *The Supernova Story*. New York: Plenum Publishing Corporation.
- Mezzacappa A. 2005. *Open Issues in Core Collapse Supernova Theory*. World Scientific Publishing Co.
- Minkowski R. 1939. *Ap.J.* 89:156.
- Minkowski R. 1940. *Pub. A.S.P.* 52:206.
- Moaz D. 2007. *Astrophysics in a Nutshell*. Princeton University Press.
- Nemiroff R, Bonnell J. 2002. *X-rays from Tycho's Supernova Remnant*. (April 2010 version). URL: <http://antwrp.gsfc.nasa.gov/apod/ap020912.html>.
- Nevalainen J, Markevitch M, Lumb D. 2005. *Ap.J.* 629:172.
- Owocki SP, Cranmer SR, Blondin JM. 1994. *Ap.J.*, 424:887.
- Revnivtsev M, Molkov S, Sazonov S. 2006. *Mon. Not. R. Astron. Soc.* 373:L11.
- Revnivtsev M, Sazonov S. 2007. *Astron. and Astro.* 471:159.
- Rho J, Petre R. 1998. *Ap.J.* 503:L167.
- Reynolds S. 1988. *Galactic and Extragalactic Radio Astronomy*.
- Reynolds S. 2008, *Annu. Rev. Astrophys.* 46:89.
- Schaaf F. 2008. *The Brightest Stars*. Hoboken, NJ: John Wiley & Sons.
- Schlegel EM. 1990. *MNRAS*. 244:269.

Slane, et.al. 2000. *Ap. J.* 533:L29.

Smith Y. 2008 in *Image of the Day Gallery*. (April 2010 version). URL: [http://www.nasa.gov/multimedia/imagegallery/image\\_feature\\_567.html](http://www.nasa.gov/multimedia/imagegallery/image_feature_567.html).

Smithsonian Institution. 2004. *Colden: Chandra X-ray Center's Proposal Planning Toolkit*. (April 2010 version). URL: <http://exc.harvard.edu/toolkit/colden.jsp>.

Snowden S, Shafer R, Smith R, Valencic L, Perry, B, Arida M. 2009. *The XMM-Newton ABC Guide: An Introduction to XMM-Newton Data Analysis*.

Walker AJ, 2006. *Filamentary H $\alpha$  structure in the Milky Way*. University of Wallongong.

Wheeler JC. Harkness RP. 1986. *Galaxy Distances and Deviations from Universal Expansion*. Dordrecht: Reidel.

Whiteoak JBZ, Green AJ. 1996. *Astron. Astrophys. Suppl. Ser.* 118:329.

Williams, DR. *Sun Fact Sheet*. (April 2010 version). URL: <http://nssdc.gsfc.nasa.gov/planetary/factsheet/sunfact.html>.